RESEARCH PAPER

ISA-Hypoplasticity accounting for cyclic mobility effects for liquefaction analysis

William Fuentes[1] · Torsten Wichtmann[2] · Melany Gil[1] · Carlos Lascarro[1]

Abstract

The hypoplastic model for sands proposed by Wolffersdorff (Mech Cohes Frict Mater 1: 251–271, 1996) combined with the intergranular strain anisotropy by Fuentes and Triantafyllidis (Int J Numer Anal Meth Geomech 39: 1235–1254, 2015) is herein extended to account for cyclic mobility effects to allow for the simulation of liquefaction phenomena. The extension is based on the introduction of an additional state variable that permits the detection of cyclic mobility paths. The simulation capabilities of the model is compared with undrained triaxial tests of Karlsruhe fine sand. At the end, a finite element simulation of an offshore monopile embedded in sand, exposed to environmental forces from the Caribbean Sea, is constructed and analyzed.

Keywords Cyclic mobility · Hypoplasticity · Intergranular strain · Liquefaction

1 Introduction

The intergranular strain anisotropy (ISA) is a mathematical extension of conventional hypoplastic models for soils (e.g., [7, 15, 17, 18, 24, 25, 46, 50, 51]) to enable the simulation of cyclic loading. It can be considered as an enhancement of the intergranular strain (IS) theory proposed by Niemunis and Herle [31] for the same purpose. Both theories are based on the introduction of a state variable, which provides information of recent changes in the strain rate direction. ISA was originally proposed by Fuentes and Triantafyllidis [11] to reproduce the following characteristics: (a) a threshold strain amplitude dividing the plastic and elastic regime; (b) the stiffness increase upon reversal loading; and (c) the reduction of the plastic strain rate for same conditions. Successful simulations of cyclic loading were achieved for a low number of repetitive cycles ($N < 10$) under undrained cyclic conditions [11]. Subsequently, an improved version of ISA was proposed in

[10, 12, 35] to simulate larger numbers of repetitive cycles ($N > 10$) upon one-dimensional and multi-dimensional paths. In particular, the hypoplastic model for sands proposed by Wolffersdorff [49] and extended by ISA, hereafter referred to as HP + ISA, has proved to capture well the accumulation of pore water pressure under undrained triaxial cycles [12, 35], but lacks congruence on the simulation of cyclic mobility effects. The latter limitation has disabled, for example, the proper simulation of the effective stress reduction on analyses related to liquefaction phenomena. So far, the cyclic mobility effect has never been tackled on hypoplastic models extended by ISA. To the authors opinion, two reasons explain the lack of this effect on these models: The first is the fact that hypoplastic models have shown to reproduce well the stress–dilatancy ratio (q / p vs. $\dot{\varepsilon}_v/\dot{\varepsilon}_s$, see notation in "Appendix A") under cyclic drained triaxial tests with constant mean stress ($p =$ const), property considered as a formal advantage of this model family by some authors [29, 51]. Modification of the constitutive equation to account for cyclic mobility effects may eventually compromise its capabilities on the mentioned property. The second is related to the fact that extensions based on the intergranular strain (IS) concept, such as [31, 45] and [11, 12, 35], are focused only on the behavior at small strain amplitudes, contrasting to cyclic

✉ William Fuentes
  fuenteslacouture1@gmail.com

1 University del Norte, Km.5 Vía Puerto Colombia, Barranquilla, Colombia

2 Ruhr-Universität Bochum, Universitätsstraße 150, 44801 Bochum, Germany

mobility effects which are exhibited on cycles of large strain amplitudes.

The present work introduces an extension of the hypoplastic model for sands proposed by Wolffersdorff [49] implementing ISA (HP + ISA) to account for cyclic mobility effects. Attention is given on the formulation to guarantee the correct assessment of the stress–dilatancy ratio (q / p vs. $\dot{\varepsilon}_v/\dot{\varepsilon}_s$) under drained triaxial $p = $ const tests. For this purpose, a strain-type state variable is proposed to provide information about the recent direction of the strain rate after reaching large strain amplitudes. With this, a mechanism to detect paths at which the cyclic mobility effect should be activated is proposed, and the hypoplastic model extended by ISA is modified to account for cyclic mobility effects. The modification is simple and introduces two additional parameters and a state variable. In addition, a modification is also introduced to improve simulations under transverse loading. The work is ended with a finite element (FE) simulation of an offshore monopile founded on a sandy soil. The simulation is performed under dynamic analysis to reproduce an extreme event typical for the Caribbean Sea. The resulting liquefaction zones of the FE model are carefully analyzed. The work begins with a brief description of the ISA-hypoplastic model. Subsequently, the proposed extension accounting for cyclic mobility effects is explained. Following this, the assessment of the proposed model on simulations of some cyclic tests is evaluated. Finally, the FE example of the offshore monopile is qualitatively analyzed. Notation and conventions adopted in the current work are given in "Appendix A".

2 Brief description of ISA-hypoplastic model

The following general form of hypoplasticity is considered in the present work:

$$\dot{\boldsymbol{\sigma}} = \mathsf{L}^{\text{hyp}} : \dot{\boldsymbol{\varepsilon}} + \mathbf{N}^{\text{hyp}} \parallel \dot{\boldsymbol{\varepsilon}} \parallel \tag{1}$$

where $\dot{\boldsymbol{\sigma}}$ is the stress rate tensor, $\dot{\boldsymbol{\varepsilon}}$ is the strain rate tensor and L^{hyp} and $\mathbf{N}^{\text{hyp}}$ are the (fourth rank) linear stiffness and (second rank) nonlinear stiffness, respectively, formulated as functions of the stress $\boldsymbol{\sigma}$ and the void ratio e only, i.e., $\mathsf{L}^{\text{hyp}} = \mathsf{L}^{\text{hyp}}(\boldsymbol{\sigma}, e)$ and $\mathbf{N}^{\text{hyp}} = \mathbf{N}^{\text{hyp}}(\boldsymbol{\sigma}, e)$. The same relation can be rewritten in terms of its continuum tangent modulus $\mathsf{M} = (\partial\dot{\boldsymbol{\sigma}})/(\partial\dot{\boldsymbol{\varepsilon}})$ as:

$$\dot{\boldsymbol{\sigma}} = \left(\mathsf{L}^{\text{hyp}} + \mathbf{N}^{\text{hyp}} \overrightarrow{\dot{\boldsymbol{\varepsilon}}}\right) : \dot{\boldsymbol{\varepsilon}} = \mathsf{M} : \dot{\boldsymbol{\varepsilon}} \tag{2}$$

Tensors L^{hyp} and $\mathbf{N}^{\text{hyp}}$ are adjusted to simulate the behavior of the soil under medium and large strain amplitudes, or equivalently, under monotonic loading [15, 17, 18, 24, 50, 51]. For this work, definitions of tensors L^{hyp} and $\mathbf{N}^{\text{hyp}}$

follow from relations proposed by Wolffersdorff [49] for sands. For paths with complex cyclic loading, Eq. 2 is not well suited, and an extension to capture small strain effects is required.

The ISA approach by Fuentes and Triantafyllidis [11], understood as an extension for hypoplastic models to enable simulations on cyclic loading, was proposed to that end. This approach is based on the concept of intergranular strain (IS), originally introduced by Niemunis and Herle [31] in a former formulation. The main difference of the ISA formulation [11] with respect to conventional IS [31], is the introduction of an elastic locus to describe the small strain behavior. According to the ISA theory, the rate of the intergranular strain $\mathbf{h}$ evolves through an elastoplastic formulation:

$$\dot{\mathbf{h}} = \begin{cases} \dot{\boldsymbol{\varepsilon}} & \text{for } F_H < 0 \quad \text{(elastic)} \\ \dot{\boldsymbol{\varepsilon}} - \dot{\lambda}\mathbf{N} & \text{for } F_H = 0 \quad \text{(plastic)} \end{cases} \tag{3}$$

where F_H is a yield surface function, $\dot{\lambda}$ is the plastic multiplier and $\mathbf{N}$ is an associated flow rule ($\mathbf{N} = \partial F_H/\partial\mathbf{h}$). The yield function F_H was formulated to consider an elastic threshold strain $\parallel \Delta\boldsymbol{\varepsilon} \parallel = R$. Considering that under elastic conditions $F_H < 0$, increments in strains are equal to increments in intergranular strain, i.e., $\Delta\boldsymbol{\varepsilon} = \Delta\mathbf{h}$ (see Eq. 3), the elastic strain amplitude is simply described through the following yield surface function F_H:

$$F_H = \parallel \mathbf{h} - \mathbf{c} \parallel -R/2 \quad \text{(yield surface)} \tag{4}$$

where tensor $\mathbf{c}$ defines the center of the yield surface (kinematic hardening variable). To account for small strain effects, the ISA approach reformulates the continuum tangent stiffness M from Eq. 2 according to the following relation:

$$\mathsf{M} = \begin{cases} m(\mathsf{L}^{\text{hyp}} + \rho^{\chi}\mathbf{N}^{\text{hyp}}\mathbf{N}) & \text{for } F_H = 0 \quad \text{(plastic)} \\ m_R\mathsf{L}^{\text{hyp}} & \text{for } F_H < 0 \quad \text{(elastic)} \end{cases} \tag{5}$$

where m is a scalar function ($1 \leq m \leq m_R$) controlling the stiffness decay upon different strain amplitudes, $m_R \geq 1$ is a parameter, ρ is a scalar function ($0 \leq \rho \leq 1$) controlling the increase of plastic strain rate for increasing strain amplitudes and χ is an exponent to control the mentioned behavior (see "Appendix C" for their definitions). These equations depend on the IS tensor $\mathbf{h}$ and other internal state variables which are carefully explained in [11, 12, 35]. Complete set of equations is given in "Appendix C" while details are found in [11, 12, 35].

One of the advantages of ISA-hypoplasticity is the ease to adapt its equation to a convenient mathematical relation depending on the strain amplitude: For small strain amplitudes ($\parallel \Delta\boldsymbol{\varepsilon} \parallel < 10^{-4}$), the response is elastic and the

model delivers $\dot{\boldsymbol{\sigma}} = m_R \mathsf{L}^{\mathrm{hyp}} : \dot{\boldsymbol{\varepsilon}}$ with ($m = m_R$, $\rho = 0$). Under medium strain amplitudes ($10^{-4} < \parallel \Delta \boldsymbol{\varepsilon} \parallel < 10^{-2}$), the transitional equation $\dot{\boldsymbol{\sigma}} = m(\mathsf{L}^{\mathrm{hyp}} + \rho^\chi \mathbf{N}^{\mathrm{hyp}}\mathbf{N}) : \dot{\boldsymbol{\varepsilon}}$ with ($0 < \rho < 1$ and $1 < m < m_R$) is rendered providing a smooth response. Finally, under large strain amplitudes $\parallel \Delta \boldsymbol{\varepsilon} \parallel > 10^{-3}$, the model coincides with the hypoplastic equation $\dot{\boldsymbol{\sigma}} = (\mathsf{L}^{\mathrm{hyp}} + \mathbf{N}^{\mathrm{hyp}}\mathbf{N}) : \dot{\boldsymbol{\varepsilon}}$ with ($m = \rho = 1$), favorable for the simulation of monotonic loading.

In Fig 1, some simulations of the degradation of the shear secant stiffness G_{sec} of the Karlsruhe fine sand are shown (parameters of Table 1). For its construction, several cyclic drained triaxial tests of different strain amplitudes were simulated, considering an initial void ratio of $e_0 = 0.85$ and different confining pressures $p_0 = \{200, 300\}$ kPa. The 5th cycle of the cyclic tests was considered for the computation of G_{sec}. For comparison purposes, the empirical relation proposed by Wichtmann and Triantafyllidis [47] based on a large number of experiments is included in Fig. 1b, see "Appendix B" for details. This empirical relation can only be considered as an approximation of the real behavior, since it depends only on the uniformity coefficient c_u, and has been calibrated on measurements with bender element tests on different sands. The results show that the estimation of G_{max} and its subsequent degradation approximately coincides with the empirical relation. It is noted, however, that the transition from elastic to plastic is not smoothly described, as by other elastoplastic models.

3 Incorporation of cyclic mobility effect

Under undrained large deformations, the dilative behavior of the material is accompanied by a strong rearrangement of particle contacts depending on the shearing direction

[6, 22]. When the shearing direction is reversed, the previous tendency to dilate is followed by a contractant behavior with positive pore pressure build-up, which causes the cyclic mobility effect. The effect has been reproduced under large shearing deformations through discrete element method (DEM) simulations, and it has been shown that during this mechanism, a strong rearrangement of particle contacts is observed [19, 28, 37, 38, 43]. For constitutive modeling purposes, some authors have shown that paths at which the cyclic mobility effect is activated can be detected through the incorporation of an additional tensorial state variable, which evolves only at large strain amplitudes exhibiting a dilatant behavior [1, 4, 6, 21, 30, 39]. Following a similar strategy, we introduce a second-rank state variable tensor, denoted by $\mathbf{Z}$, which provides information related to the recent history of the shearing loading direction under large strain amplitudes. For convenience, the shearing loading direction is in this work described by the IS flow rule tensor $\mathbf{N}$, considering that under monotonic paths, the relation $\mathbf{N} = \vec{\boldsymbol{\varepsilon}}$ holds [9, 11]. Hence, a suitable relation for the evolution equation of tensor $\mathbf{Z}$ is:

$$\dot{\mathbf{Z}} = c_z \langle F_d \rangle (\mathbf{N} - \mathbf{Z}) \parallel \dot{\boldsymbol{\varepsilon}} \parallel \tag{6}$$

where c_z is a material constant, the operators $\langle \ \rangle$ are the Macaulay brackets ($\langle \cup \rangle = \cup$ for $\cup > 0$ and $\langle \cup \rangle = \cup = 0$ otherwise), and F_d is a scalar function to be defined. Notice that the general form of Eq. 6 is similar as in other works [1, 4, 6, 21, 39]. Accordingly, factor $\langle F_d \rangle$ is only different from zero for positive values of F_d. For the sake of convenience, F_d is a positive function ($F_d > 0$) only when the strain amplitude is sufficiently large to activate the rearrangement of the particle contacts producing a dilatant behavior under triaxial shearing. Some constitutive models have proposed the use of a "dilatancy surface function" for
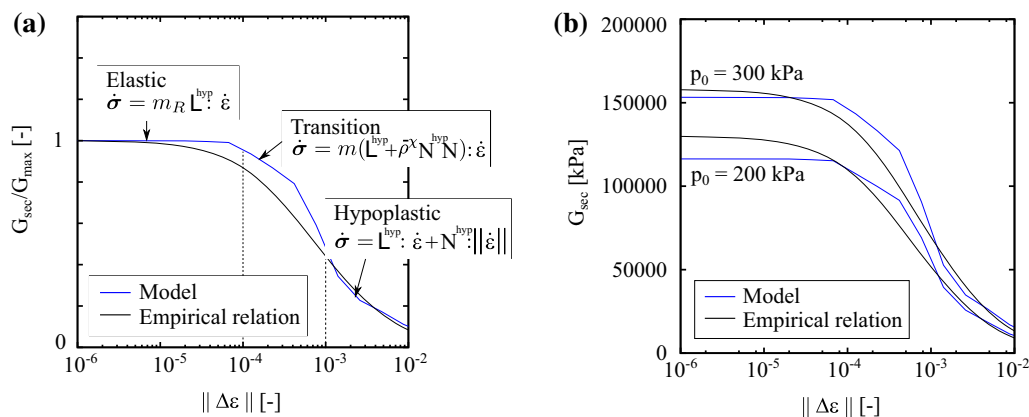

Fig. 1 Simulation of the degradation curve of the shear secant stiffness G_{sec} with ISA-hypoplasticity. Empirical relation by [47]. **a** $G_{\mathrm{sec}}/G_{\mathrm{max}}$ versus $\parallel \Delta \boldsymbol{\varepsilon} \parallel$, and sketch of model response. **b** Simulation against empirical relation by [47]. Karlsruhe fine sand. Parameters from Table 1. Initial void ratio $e_0 = 0.85$

Table 1 Parameters of proposed model (HP+ISA) for Karlsruhe fine sand

Parameter	Nomenclature	Value	Units
Critical state friction angle	φ_c	32.6	°
Granular hardness	h_s	4.000.000	kPa
Barotropy exponent	n_B	0.27	–
Minimum void ratio at $p = 0$ kPa	e_{d0}	0.677	–
Critical void ratio at $p = 0$ kPa	e_{c0}	1.054	–
Maximum void ratio at $p = 0$ kPa	e_{i0}	1.212	–
Dilatancy exponent	α	0.14	–
Pyknotropy exponent	β	2.5	–
Stiffness factor	m_R	5.0	–
Elastic strain amplitude	R	1.4×10^{-4}	–
Minimum IS hardening parameter	β_{h0}	0.25	–
Maximum IS hardening parameter	β_{hmax}	3.0	–
Minimum IS exponent	χ_0	5	–
Maximum IS exponent	χ_{max}	17.7	–
Accumulation rate factor	c_a	0.018	–
Cyclic mobility factor	c_z	300	–

F_d, defined as the surface in the stress space at which the plastic volumetric strains ε_{ii}^p turn from contractant ($\dot{\varepsilon}^p_{ii} < 0$) to dilatant ($\dot{\varepsilon}^p_{ii} > 0$) upon triaxial shearing, i.e., $F_d = 0$ when $\dot{\varepsilon}^p_{ii} = 0$. This is convenient for conventional elastoplastic models, because it coincides with the phase transformation line observed under undrained triaxial shearing, which is dependent on the current stress $\boldsymbol{\sigma}$ and void ratio e according to experimental observations [20]. However, hypoplastic models do not incorporate directly such surface on its formulation considering that there is no explicit definition of a plastic strain rate. Indeed, the resulting contractancy–dilatancy behavior under undrained triaxial shearing depends on both tensors $\mathbf{L}^{hyp}$ and $\mathbf{N}^{hyp}$ and not on an explicitly defined flow rule as by some elastoplastic models[1]. After a careful inspection of the simulations with the hypoplastic model by Wolffersdorff [49], we propose the following simple function for F_d suited to detect large strain amplitudes responsible for the dilatant behavior under undrained triaxial shearing:

---

[1] On the other hand, Wu and Niemunis [52] showed that the direction of tensor $\mathbf{m} = -(\mathsf{L}^{hyp})^{-1} : \mathbf{N}^{hyp}$ coincides with the one of the accumulated strain under a closed infinitesimal stress cycle, which may be interpreted by some authors as a hypoplastic flow rule [11, 29, 52]. However, one may also show that its resulting dilatancy surface described by the condition $m_{ii} = 0$ coincides with the critical state surface, which does not depend on the void ratio and therefore disagrees with experiments, see "Appendix D"

$$F_d \equiv \frac{q/p}{M_c F f_{d0}} - 1 = 0 \tag{7}$$

where q is the deviator stress, p is the mean (effective) stress, $M = M_c F = 6 \sin(\varphi_c)/(3 - \sin \varphi_c)F$ is the critical state slope in the $q - p$ space, f_{d0} is the pyknotropy factor [49], F is a scalar function controlling the Matsuoka–Nakai shape of the critical state surface [26] and is defined in Eq. 39, and φ_c is the critical state friction angle. Note that Eq. 7 depends on factor f_{d0} and therefore on the void ratio e. Equation 7 does not represent exactly the phase transformation line (PTL), but has proved to be a good approximation of this line on simulations of undrained triaxial tests with hypoplasticity. This is shown in Fig. 2 which presents simulation examples of undrained triaxial tests with different void ratios using parameters of Table 1. The curve resulting from the relation $F_d = 0$, see Eq. 7, has been also included for comparison purposes.

We now proceed to formulate a scalar factor aiming to detect paths at which the cyclic mobility effect should be active. To that end, the scalar factor f_z depending on tensor $\mathbf{Z}$ is introduced:

$$f_z = \langle -\mathbf{Z} : \mathbf{N} \rangle \tag{8}$$

Note that factor f_z is bounded by $0 \leq f_z \leq 1$. A value of $f_z = 0$ indicates that the effect of the cyclic mobility is negligible, while a value of $f_z = 1$ means that it must be fully considered. Intermediate values of $0 < f_z < 1$ would intend to describe a transition between these two states. In this sense, factor f_z controls the intensity at which the cyclic mobility effect should be considered.

Having factor f_z defined, an extension to the ISA + HP model is now carefully proposed to account for cyclic mobility effects. Under a cyclically mobilized path, factor f_z is greater than zero, i.e., $f_z > 0$, and a more contractant behavior should be simulated. It will be shown that this contractant effect can be simply captured if a similar contractant behavior of the material as by its loose state is delivered, i.e., $e \approx e_c$, where e_c is the critical state void ratio. Considering this, the following mathematical statements are proposed to be fulfilled:

- For cyclic mobility states with $f_z = 1$, the scalar factors f_e and f_d are set to one, i.e., $f_e = f_d = 1$. Note that this is similar to replace $e = e_c$ at the original definitions of factors f_e and f_d (see Eqs. 38).
- For same conditions ($f_z = 1$), the effect of the intergranular strain must be reduced to avoid an excessively stiff behavior on cyclic mobility paths.

To fulfill the first requirement, the scalar factors f_e and f_d are modified according to the following relations:
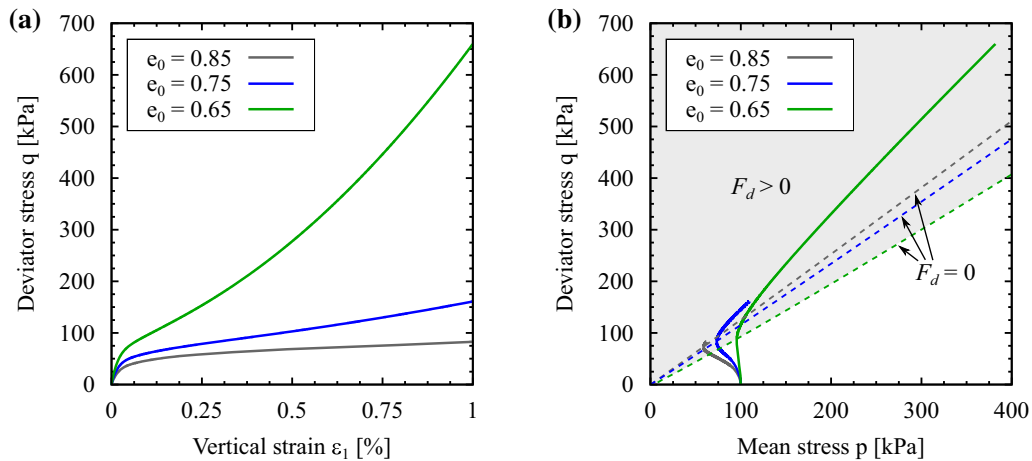
Fig. 2 Simulations of undrained monotonic triaxial compression tests. Variation of the void ratio. **a** q versus ε_1 space. **b** q versus p space, the curve $F_d = 0$ from Eq. 7 is depicted and coincides approximately with the phase transformation line

$$f_e = f_{e0} - f_z\langle f_{e0} - 1\rangle, \quad \text{with} \quad f_{e0} = \left(\frac{e_c}{e}\right)^\beta \quad (9)$$

$$f_d = f_{d0} + f_z\langle 1 - f_{d0}\rangle, \quad \text{with} \quad f_{d0} = \left(\frac{e - e_d}{e_c - e_d}\right)^\alpha \quad (10)$$

where $e_d = e_d(p)$ is the minimum void ratio (see "Appendix C"), and α and β are material parameters. Note that for $f_z = 1$, both factors render $f_e = f_d = 1$, and consequently a contractant behavior as by loose sand is reproduced. For $f_z = 0$ their original formulations $f_e = f_{e0}$ and $f_d = f_{d0}$ are recovered.

For the second requirement, factor β_h is reformulated aiming to reduce the strain amplitude at which the IS effect acts. Increasing the value of β_h would reduce the IS effect avoiding a stiff behavior on cyclic mobility paths. In the original model, factor $\beta_h = \beta_{h0}$ is set to a constant for all cases, however, we propose the following relation for β_h to provide the desired response:

$$\beta_h = \beta_{hmax} + (\beta_{h0} - \beta_{hmax})(1 - f_z)f_h \quad (11)$$

where f_z was previously defined in Eq. 8, f_h is a function, and β_{hmax} and β_{h0} are material parameters controlling the maximum and minimum values of $\beta_{h0} \leq \beta_h \leq \beta_{hmax}$, respectively. Under the assumption of $f_h = 1$, the lack of cyclic mobility effects $f_z = 0$ would give $\beta_h = \beta_{h0}$, while for the opposite case $f_z = 1$, the relation $\beta_h = \beta_{hmax}$ holds. It will be shown that this would reduce the effect on cyclic mobility paths. Function f_h has been additionally introduced to improve simulations on transverse loading. Accordingly, a value of $f_h = 1$ is only obtained on reverse loading (one-dimensional cycles), such as cyclic undrained triaxial tests. For other cases, as for example transverse loading, values within the range $0 \leq f_h < 1$ are obtained. Considering this, the following function has been proposed:

$$f_h = |\overrightarrow{\dot{\boldsymbol{\varepsilon}}} : \overrightarrow{\mathbf{d}_b}|, \qquad \overrightarrow{\mathbf{d}_b} = (R\overrightarrow{\dot{\boldsymbol{\varepsilon}}} - \mathbf{h})^{\rightarrow} \quad (12)$$

where $R\overrightarrow{\dot{\boldsymbol{\varepsilon}}}$ is the image of tensor $\mathbf{h}$ mapped by $\overrightarrow{\dot{\boldsymbol{\varepsilon}}}$ at the IS bounding surface, and R is a parameter. Hence, it gives $f_h = 1$ only for one-dimensional cycles, because $|\overrightarrow{\dot{\boldsymbol{\varepsilon}}} : \overrightarrow{\mathbf{d}_b}| = 1$ holds. Otherwise, factor f_h gives $f_h < 1$. A special case of transverse loading is depicted in Fig. 3, corresponding to undrained triaxial shearing after isotropic compression. One may note that the new parameter β_{hmax} controls the behavior of the $q - p$ path at the beginning of the curve. This would allow the calibration of β_{hmax} by trial and error on such curves.

Figure 4 shows a simple simulation example to illustrate the evolution of $\mathbf{Z}$. It consists of a cyclic undrained triaxial test (initial conditions $e_0 = 0.8$, $p_0 = 100$ kPa, parameters from Table 1), with constant deviator stress amplitude $q^{amp} = 60$ kPa. Figure 4a, b (q vs. ε_1 and q vs. p) shows that for such simulation, the material requires only 4 cycles to activate the cyclic mobility effect. According to Eqs. 6 and 7, tensor $\mathbf{Z}$ evolves toward $\mathbf{N}$ when $F_d > 0$ (see Fig. 2). This can be noted in Fig. 4c, where close to the 4*th* cycle, the evolution of $\mathbf{Z}$ is activated. The cyclic mobility effect is considered in the model when the condition $f_z = \langle -\mathbf{Z} : \mathbf{N}\rangle > 0$ holds, which usually occurs on paths after reversal loading ($\mathbf{Z} : \mathbf{N} < 0$).

The extended model requires the calibration of the new parameters c_z and β_{hmax}. While β_{hmax} can be calibrated on transverse loading paths, as depicted in Fig. 3, c_z can be calibrated on the butterfly-shaped loops exhibited on undrained triaxial cycles, as shown in Fig. 5. In this figure, a cyclic undrained triaxial test with constant deviator stress amplitude ($q^{amp} = 40$ kPa) has been simulated with $c_z = 0$ and $c_z = 300$. For instance, parameters of Table 1 have been borrowed. One may intermediately note the ability of the model to reproduce cyclic mobility effects with the new extension through the selection $c_z = 300$.
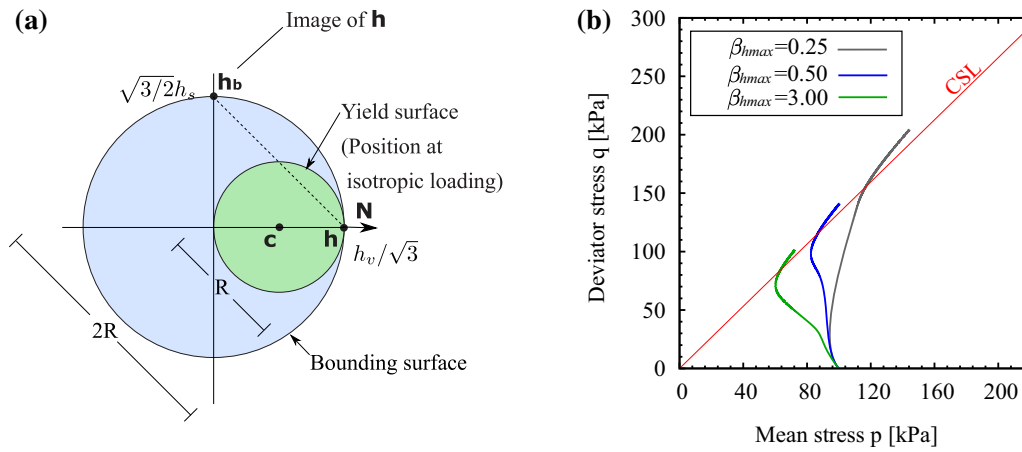
Fig. 3 The mechanism of transverse loading is schematized. **a** position of the IS yield surface and internal variables at transverse loading (undrained shearing after isotropic compression). **b** simulations of undrained triaxial tests with variation of parameter β_{hmax}
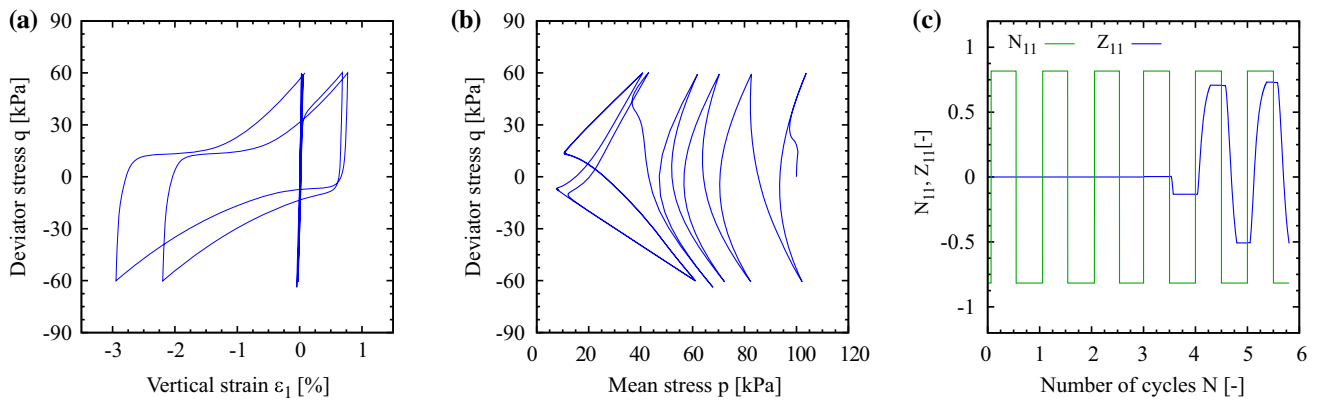

Fig. 4 Simulation example of cyclic undrained triaxial test ($e_0 = 0.8$, $p_0 = 100$ kPa, $q^{\mathrm{amp}} = 60$). Parameters from Table 1. **a** q versus ε_1. **b** q versus p. **c** Z_{11} and N_{11} versus N
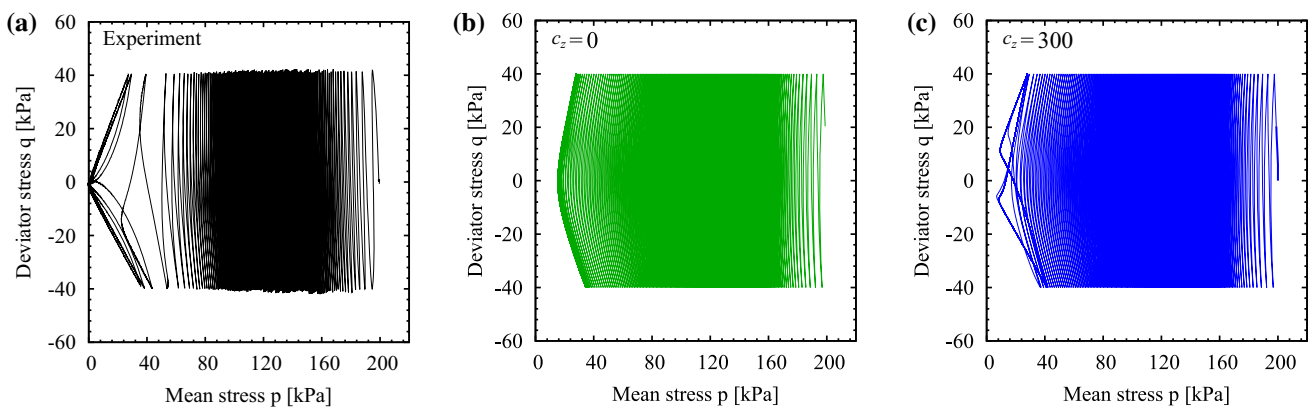
Fig. 5 Simulation of cyclic undrained triaxial test with variation of c_z. Karlsruhe fine sand parameters. $p_0 = 200$ kPa. **a** Experiment by [48] **b** $c_z = 0$, **c** $c_z = 300$

4 Simulation of element tests

Some simulations of element tests (homogeneous stress–strain field assumption) of a sand are now shown with the proposed model. The testing sand corresponds to the Karlsruhe fine sand, previously analyzed in other works [12, 35, 48]. The selected parameters are summarized in Table 1 and were found as follows: parameters of the hypoplastic model without extension (φ_c, h_s, n_B, e_{d0}, e_{c0}, e_{i0}, α, β) were directly adopted from the calibration performed in [48]. Parameters R, m_R are the same reported by Poblete et al. [35] for the same material. Parameters χ_0, χ_{max}, β_{h0}, c_a were found following the calibration guide proposed in [35] to improve their accuracy on simulations, while the new parameters c_z, β_{hmax} were calibrated according to the explanation given in Sect. 3. The numerical implementation developed in [35], written in FORTRAN code under the syntax of the subroutine UMAT from the commercial software ABAQUS Standard, has been herein extended to account for the cyclic mobility effects according to the relations of Sect. 3. The implementation was performed in the following way: A substepping scheme, with very small strain subincrements ($\| \Delta \varepsilon \| < R/4$), was implemented to achieve numerical convergence. For the intergranular strain model, which now is elastoplastic, a trial step as elastic predictor is performed in order to check the yield condition $F_H = 0$. The relations were explicitly implemented within the substepping scheme and delivered for all cases numerical convergence. Details of numerical implementation of hypoplastic models can be found in [44]. Analysis of the performance of the model under monotonic loading is out of the scope of the present work, but some simulations of oedometric tests and undrained triaxial tests with monotonic loading for different densities are included in "Appendix E" and showed to capture fairly well the behavior. Similar simulations of monotonic loading can be also found in [48].

Before comparing the model with the experiments, we begin with a simple simulation of a drained triaxial test under constant mean pressure $p = $ constant (such as by [36]). As mentioned before, this permits to evaluate the stress–dilatancy response under such conditions. The test is performed under $p = 100$ kPa (constant), with an initial void ratio of $e_0 = 0.600$ (dense state). Three different simulations are presented in Fig. 6, where the variation of parameter $c_z = \{0, 100, 300\}$ is considered. From the results, one may note that increasing values of c_z deliver a higher degradation of the shear stiffness accompanied with an increase of compressive volumetric strains, see Fig. 6.a, b and c. Hence, one may also calibrate c_z by trial and error through drained tests as an alternative. Figure 6.d presents

the stress–dilatancy response within the space of q / p versus $\dot{\varepsilon}_v/\dot{\varepsilon}_s$. The results show that the response of the model is bounded by two lines independently of parameter c_z, as shown by experiments [5, 36, 53].

Simulations of cyclic undrained triaxial tests with constant deviator stress amplitudes are shown in Fig. 7, while their pore pressure accumulation p_w^{acc} against the number of cycles is presented in Fig. 8. Three different tests with equal confining pressure $p_0 = 200$ kPa but slightly different void ratios $e = \{0.800, 0.813, 0.842\}$ were considered. The deviator stress amplitudes q^{amp} are different on each test, and correspond to $q^{amp} = \{60, 50, 40\}$ kPa. The butterfly-shaped effective stress paths during the last cycles were satisfactorily simulated by the model while the pore pressure accumulation was also well captured. In Fig. 8, it is noted that the accumulation of the pore water pressure p_w is successfully captured. The accumulation rate of the pore water pressure $\dot{p}_w^{acc}$ gradually decreases, while it grows again on the last cycles. This effect was achieved due to the enhancement of the ISA-hypoplastic model proposed by Poblete et al. [35], whereby exponent χ controlling the accumulation rate of p_w^{acc} changes gradually from χ_0 to χ_{max} to capture such effect (see Eqs. 34 and 35). The increase on the last cycles is captured due to the development of large strains, where exponent χ is again reduced to $\chi = \chi_0$, see Eq. 34. Details of this mechanism are found in [35].

Lastly, we show some simulations of undrained triaxial tests with constant axial strain amplitude $\varepsilon_1^{amp} = 0.01$. Considering that the strain amplitude is large, cyclic mobility effects are expected. Two different void ratios e_0 were considered: the first with $e_0 = 0.804$ and the second with $e_0 = 0.698$. Experiments and simulations with $c_z = 0$ and $c_z = 300$ are shown in Figs. 9 and 10. Simulations without the proposed extension ($c_z = 0$) show that the model is not able to reduce properly the mean pressure p under undrained cycles with large strain amplitudes (e.g., $\varepsilon_1^{amp} = 0.01$). Actually, for the dense case ($e = 0.698$ in Fig. 10), the mean pressure p increases for $c_z = 0$. The observed limitations are overcome when using the current extension ($c_z = 300$).

5 Simulation example of an offshore monopile

We now present a simulation example of an offshore turbine–monopile system founded on a sand. The structure is subjected to environmental loads typical for an extreme storm event. The FE model is three-dimensional and has been built using the software ABAQUS Standard. Its dimensions follow from the reference geometry NREL 5-MW established in [16] and are shown in Fig. 11. The
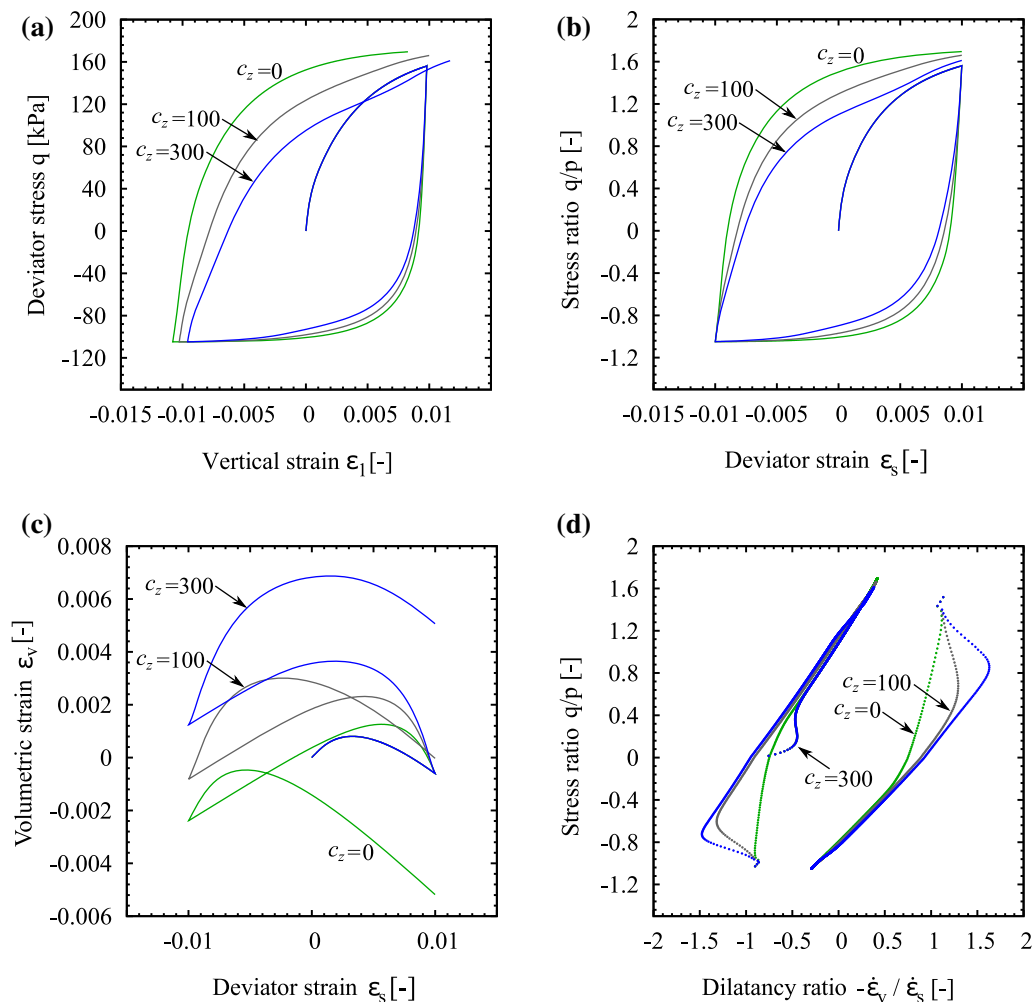
Fig. 6 Simulation of a $p = $ const triaxial test under drained conditions. Karlsruhe fine sand parameters. $p_0 = 100$ kPa

structure is founded on a steel monopile embedded in an homogeneous sand, with an embedment length of $L_p = 30$ m, diameter of $D_p = 6$ m and wall thickness of $t_p = 0.06$ m. The water depth above the mudline is of $d = 20$ m. The tower height above the mean sea level (MSL) is 87.6 m, while the hub height is 90 m. Other important properties of the geometry and weights of the different parts of the model are given in Table 2.

The discretized model is shown in Figs. 12 and 13. The FE model consists of six main parts, namely tower, substructure, monopile, soil inside the monopile, soil around the monopile and a surrounding part of soil with large finite elements to permit an appropriate numerical wave dissipation. The substructure has the same diameter and wall thickness as the monopile. In contrast, the tower presents a diameter and wall thickness which gradually reduces from 6 m at the base to 3.87 m at the top and from 0.027 m at the base to 0.019 m at the top, respectively. The foundation and the structure were modeled with four-node shell

elements and the soil domain with eight-node brick elements and six-node wedge elements. The turbine rotor and nacelle were considered through lumped masses located at their corresponding centers of mass, see Table 2.

Rigid constraints were set between the monopile, substructure and tower to consider it as a continuum structure. The soil–monopile interface behavior was customized through a small sliding surface-to-surface interaction configuration. The frictional behavior was controlled using a penalty method with a coefficient of friction assumed as $\mu = 0.3$. The normal behavior was controlled with a hard contact relation which allows any pressure to be transmitted between surfaces in contact.

The material used for the monopile and the structure was simulated through a linear elastic model representing the steel, with an elastic modulus of $E = 210$ GPa and Poisson ratio of $v = 0.3$. As recommended by Jonkman et al. [16], a density of 8500 kg/m³ was used in order to account for the weight of paint, bolts, welds and flanches. The material model for the soil corresponds to the extended
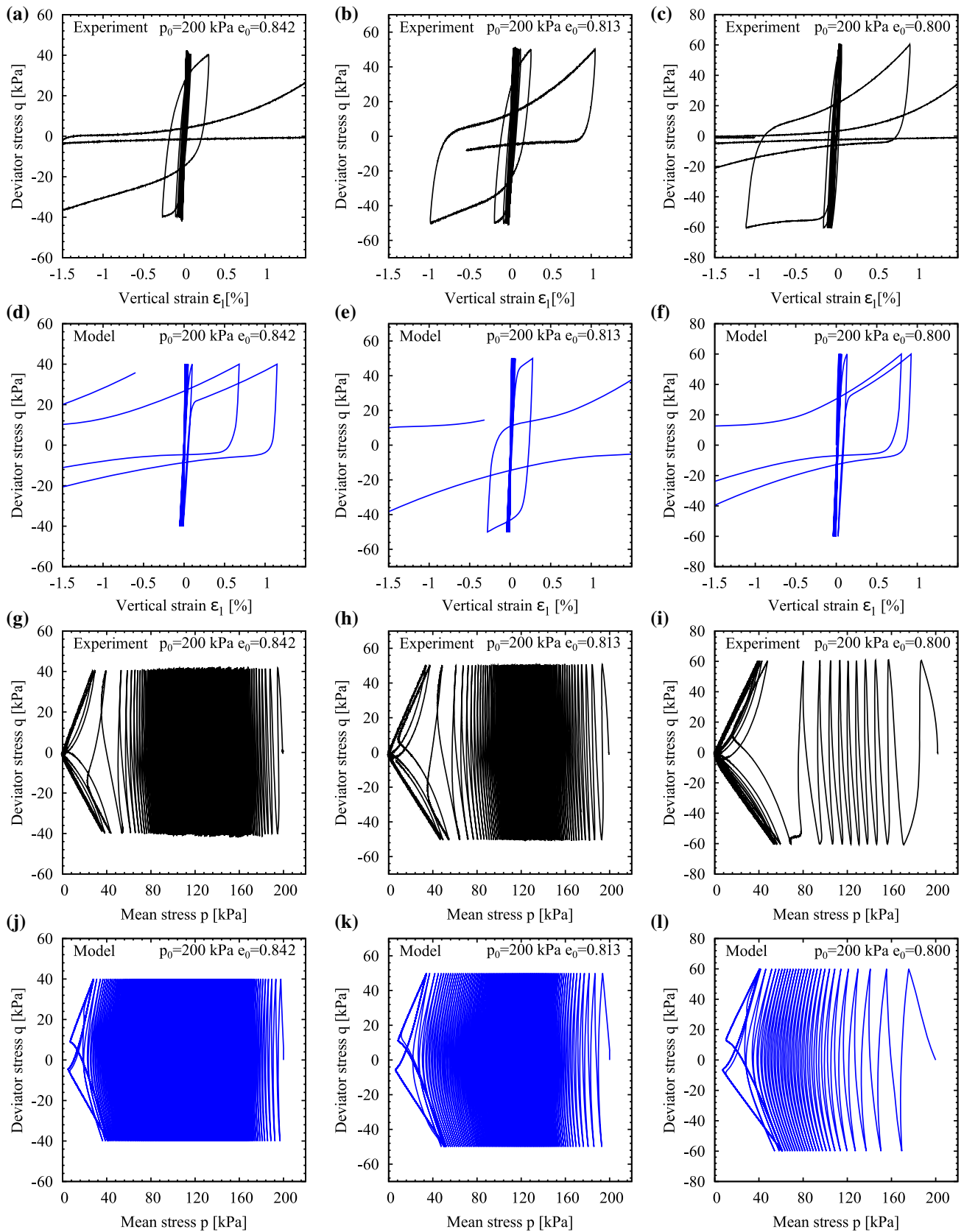
Fig. 7 Simulation of cyclic undrained triaxial tests with different deviator stress amplitudes in the q versus ε_1 and q versus p space. Karlsruhe fine sand. **a** $q^{amp} = 40$ kPa, **b** $q^{amp} = 50$ kPa, **c** $q^{amp} = 60$ kPa. Experiments by [48]
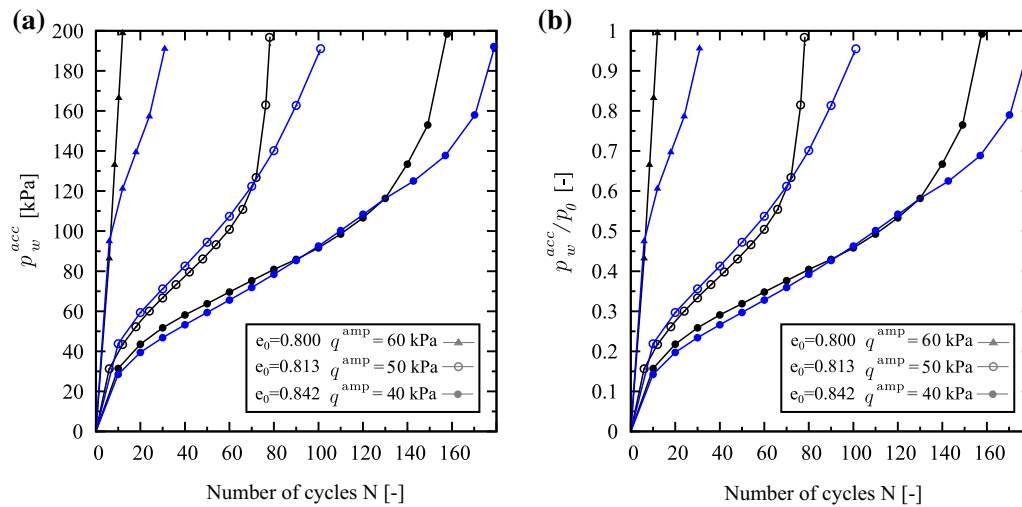
Fig. 8 Simulation of cyclic undrained triaxial tests with different deviator stress amplitudes. Accumulation of pore water pressure. Karlsruhe fine sand. $p_0 = 200$ kPa. Experiments by [48]
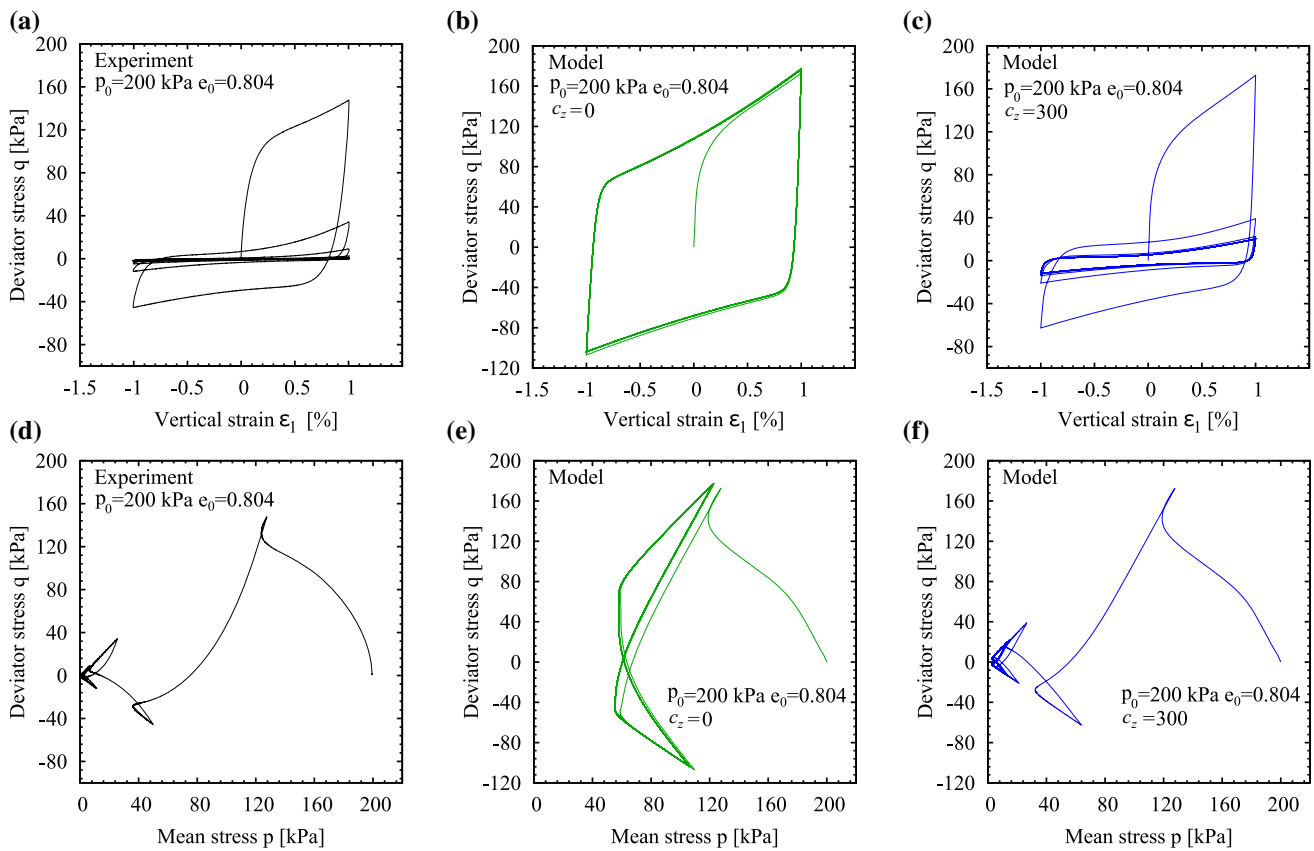

Fig. 9 Simulation of cyclic undrained triaxial test with variation of c_z. $c_z = 0$ indicates the proposed model without cyclic mobility effects, whereas $c_z = 300$ implies simulation of this effect. Constant axial strain amplitude $\varepsilon_1^{amp} = 0.01$ and void ratio of $e_0 = 0.804$. Karlsruhe fine sand. $p_0 = 200$ kPa. Experiments by [48]

ISA-hypoplastic model of the present work, calibrated for the Karlsruhe fine sand according to parameters in Table 1.

5.1 Description of loads

Offshore wind turbines are subjected to a combination of loads mainly caused by the action of wind and waves and
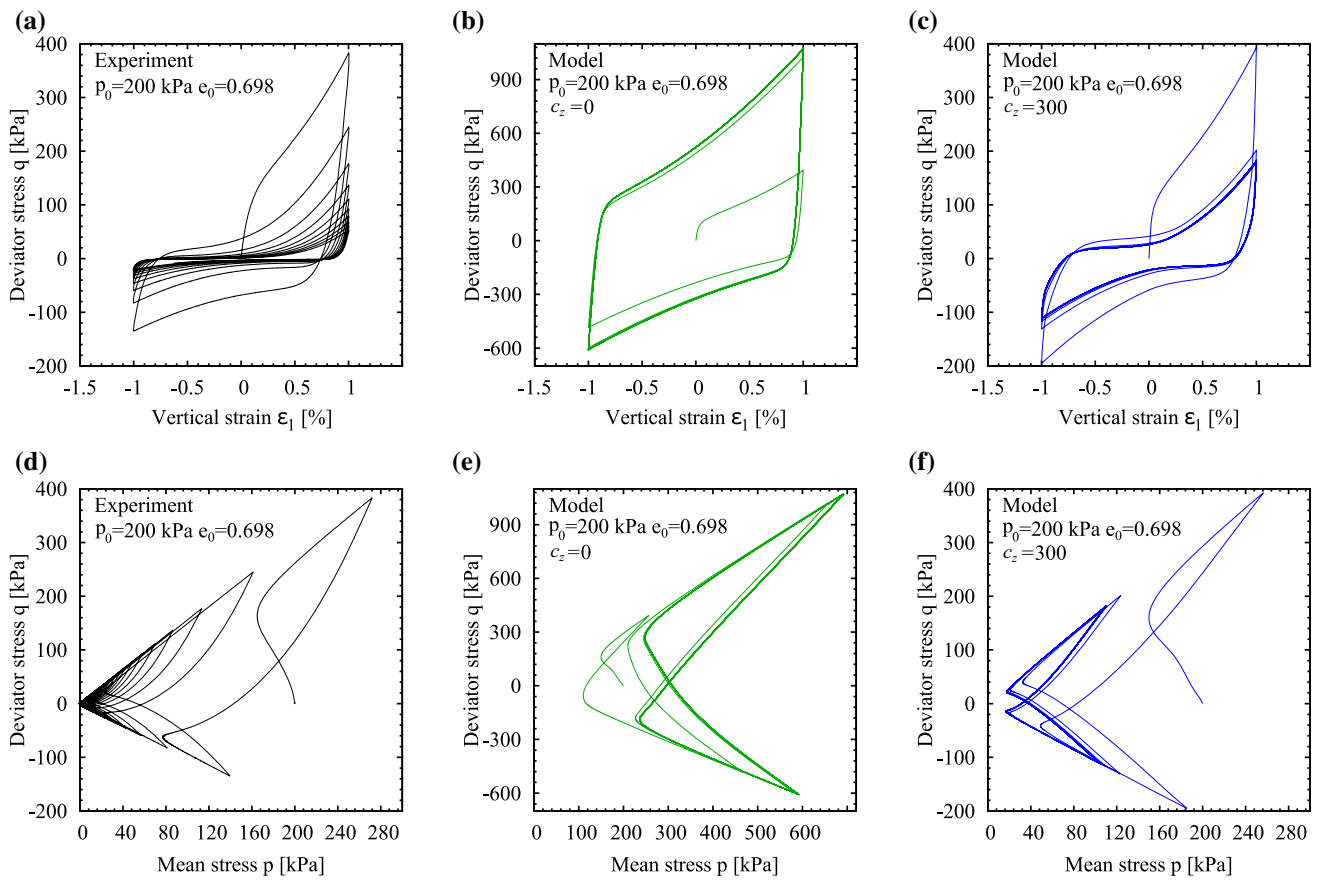
Fig. 10 Simulation of cyclic undrained triaxial test with variation of c_z. $c_z = 0$ indicates the proposed model without cyclic mobility effects, whereas $c_z = 300$ implies simulation of this effect. Constant axial strain amplitude $\varepsilon_1^{amp} = 0.01$ and void ratio of $e = 0.698$. Karlsruhe fine sand. $p_0 = 200$ kPa. Experiments by [48]
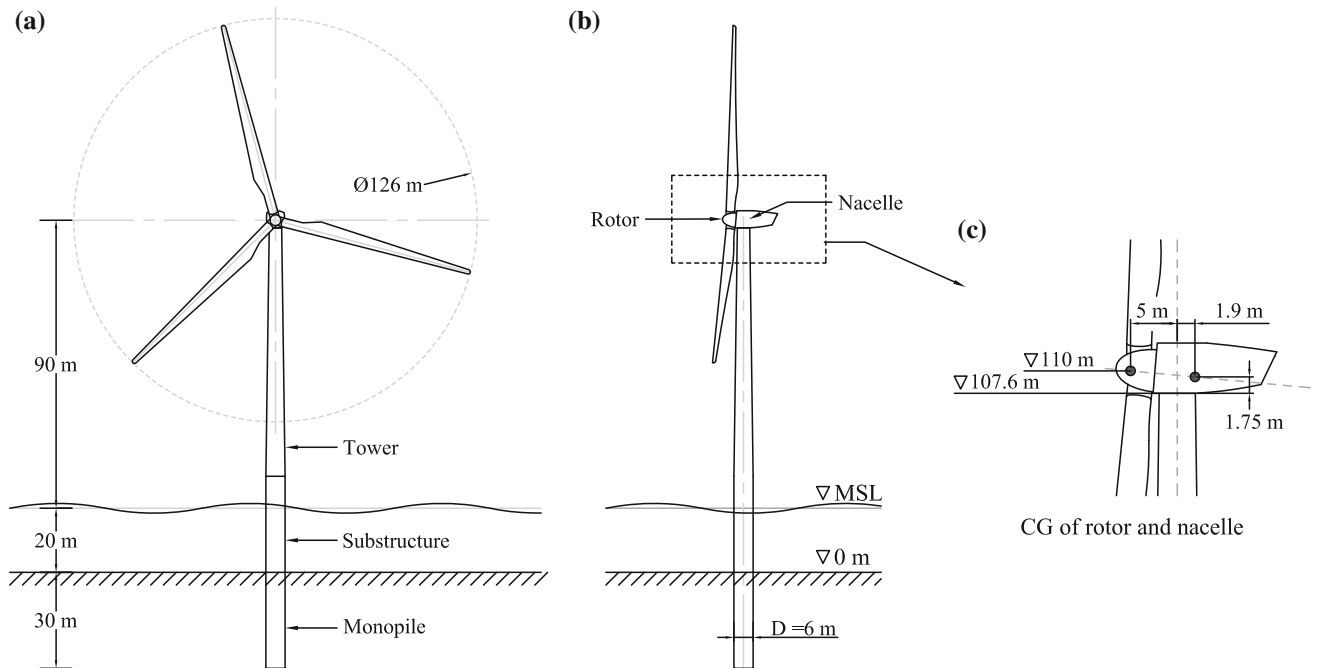

Fig. 11 Offshore wind turbine conceptual model and geometry

Table 2 Properties of the finite element model

Property	Value	Units
Mean sea level (MSL)	20.0	m
Hub height above MSL	90.0	m
Tower top height above MSL	87.6	m
Pile embedment depth	30.0	m
Pile diameter	6.0	m
Pile wall thickness	0.06	m
Rotor mass	110,000	kg
Nacelle mass	240,000	kg

the self-weight of the structure. Other type of loads acting on the structure is caused by currents, aerodynamic imbalances at the hub level and blade shadowing effects [3]. However, a simplified estimation of the environmental loads that only accounts for the wind and wave action is here adopted as shown in Fig. 14. The wind and wave loads are assumed as codirectional and are estimated considering the site conditions of the Colombian Caribbean Sea. Following the findings in [8], a typical extreme event in the Colombian Caribbean Sea for offshore applications could be defined by a surface wind speed at the height of 10 m above the mean sea level (U_{10m}) between 15 and 20 m/s,
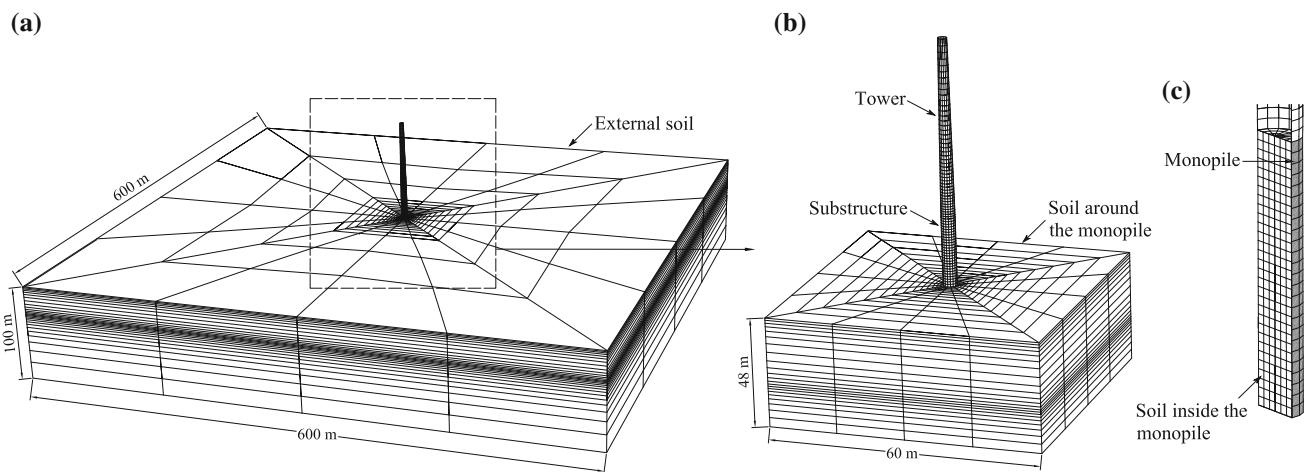

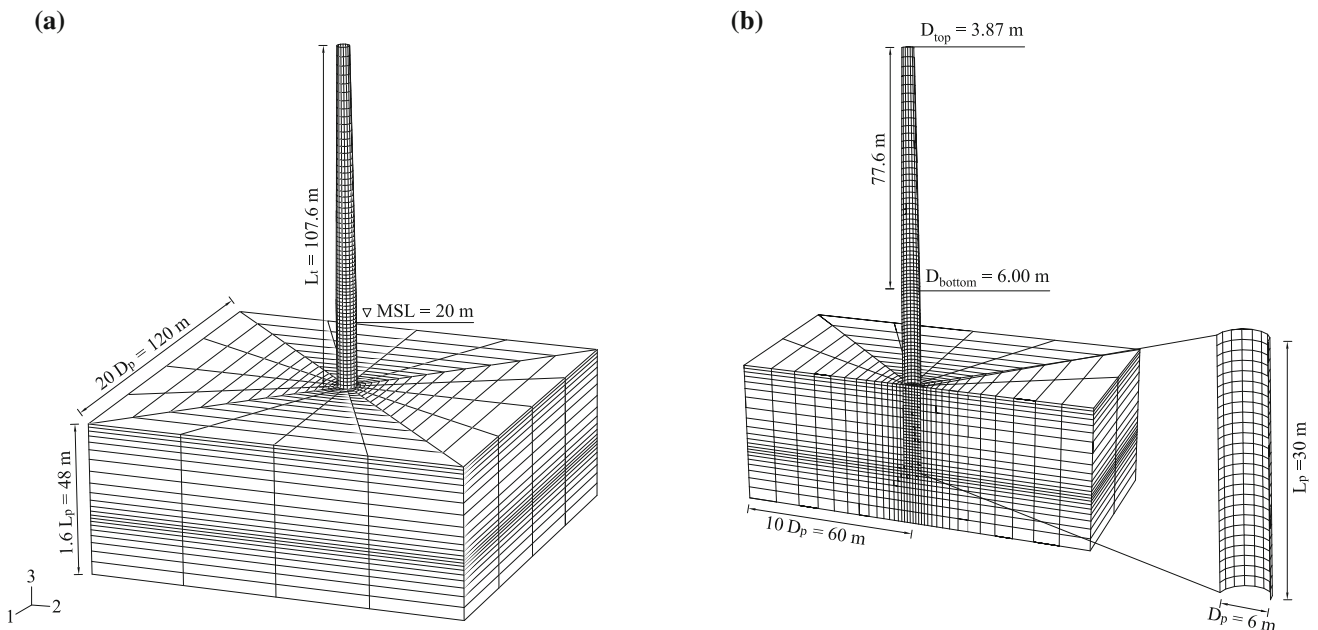**Fig. 12** Main parts and mesh of the 3D finite element (FE) model

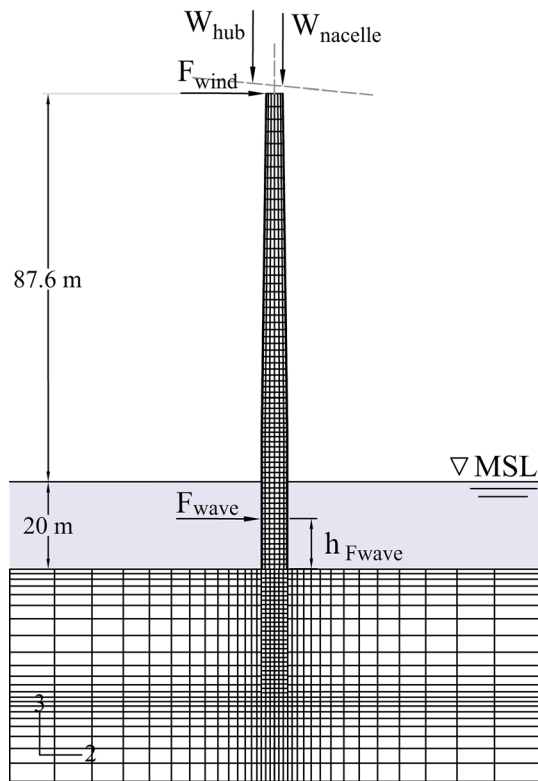**Fig. 13** Geometry of the 3D finite element (FE) model

Fig. 14 Loads applied on the structure

and a significant wave height with values between $H_s > 3$ m for nearshore locations and $H_s > 5$ m for other locations in the Caribbean Sea. For this work, the following environmental parameters were chosen: $U_{10m} = 17$ m/s and $H_s = 6$ m. In addition, the sea state was also defined by a wave spectral peak period of $T_p = 8$ s [34]. These values are considered to be conservative and simulate a storm in the Colombian Caribbean Sea.

The wind thrust force F_{wind} is calculated by applying the momentum theory to an idealized one-dimensional model of the wind turbine (see more details in [14]). Thus, the following relation results:

$$F_{wind} = \frac{1}{2}\rho_a A_r C_T U_{hub}^2 \qquad (13)$$

where $\rho_a = 1.22$ kg/m³ is the density of the air, A_r is the rotor swept area of the NREL reference turbine [16], U_{hub} is the wind speed at the hub level and C_T is a thrust coefficient, the latter defined later on. The wind speed U_{hub} is estimated from U_{10m} using a logarithmic wind speed profile:

$$U(z) = U(z_{ref}) \frac{\ln z - \ln z_0}{\ln z_{ref} - \ln z_0} \qquad (14)$$

where $U(z)$ is the wind speed located at height z, z_{ref} is a reference height, which in this case is $z_{ref} = 10$ m, $U(z_{ref})$ = U_{10m} is the wind speed at the reference height, and z_0 is

the surface roughness length. For blown sea conditions, the value of z_0 can be assumed as 0.0005 m [23]. Hence, following Eq. 14 the obtained wind speed at the hub level is $U_{hub} = 20.8$ m/s.

On the other hand, an approximate value of the thrust coefficient C_T may be computed as a function of the tip speed ratio (λ) [13, 41]. For the obtained value of U_{hub}, Jonkman et al. [16] report $\lambda = 4$. From this, [13] gives $C_T = 0.5$. Improved calibration of the factor C_T may be obtained through sophisticated aerodynamic simulations (see Example in [32]), but this is beyond the scope of the present work. Finally, the wind thrust force F_{wind} is calculated using Eq. 13 and is plotted in Fig. 15 against time.

In addition, the hydrodynamic load is estimated using a simplified method proposed by [40, 42]. A calculation based on the Airy linear wave theory and the Morison equation [27] is used to obtain the inertial and drag components of the hydrodynamic force and overturning moment (Eqs. 15–18). The inertial components of the hydrodynamic force and overturning moment are denoted by F_{wave}^I and M_{wave}^I, respectively, while the drag components are denoted by F_{wave}^D and M_{wave}^D, and read:

$$F_{wave}^I = \rho_w g H_s \frac{C_m \pi D_p^2}{8} \tanh(kd) \qquad (15)$$

$$F_{wave}^D = \rho_w g H_s^2 \frac{C_d D_p}{8}\left[\frac{1}{2} + \frac{kd}{\sinh(2kd)}\right] \qquad (16)$$

$$M_{wave}^I = \rho_w g H_s \frac{C_m \pi D_p^2}{8} d\left[\tanh(kd) + \frac{1}{kd}\left(\frac{1}{\cosh(kd)} - 1\right)\right] \qquad (17)$$

$$M_{wave}^D = \rho_w g H_s^2 \frac{C_d D_p}{8}\left[\frac{d}{2} + \frac{2(kd)^2 + 1 - \cosh(2kd)}{4k\sinh(2kd)}\right] \qquad (18)$$

where $\rho_w = 1000$ kg / m³ is the water density, $g = 9.81$ m / s² is the gravitational acceleration, $H_s = 6$ m is the significant wave height, C_m and C_d are the inertia and drag coefficients, and k is the wave number. The latter can be determined by iterative procedures using the relation $\omega^2 = gk\tanh(kd)$, where $\omega = 2\pi f_s$ is the wave circular frequency and $f_s = 1/T_p$. The values for the inertia and drag coefficients are assumed as $C_m = 1.6$ and $C_d = 0.65$, respectively, following the recommendations in [2]. The total wave force F_{wave} and moment M_{wave} acting on the structure read:

$$F_{wave}(t) = \sqrt{(F_{wave}^I)^2 + (F_{wave}^D)^2} \sin \omega t \qquad (19)$$

$$M_{wave}(t) = \sqrt{(M_{wave}^I)^2 + (M_{wave}^D)^2} \sin \omega t \qquad (20)$$
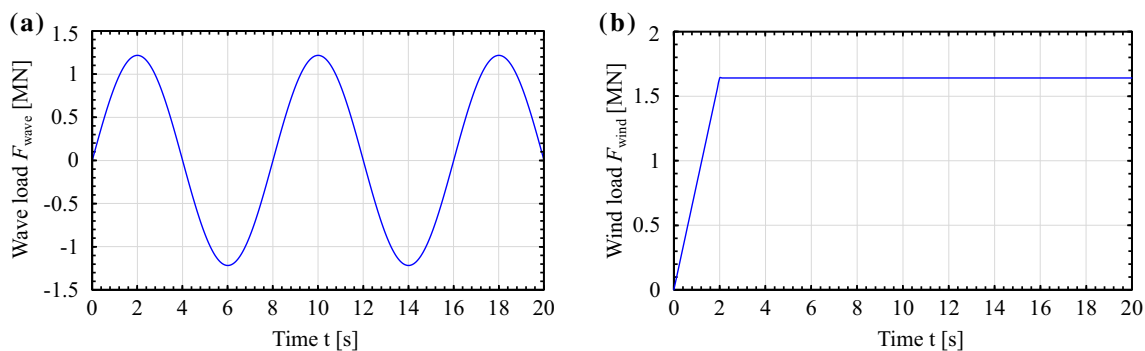
Fig. 15 Time histories of the wind and wave loading

Finally, the equivalent hydrodynamic loading is incorporated in the FE problem by applying $F_{\text{wave}}(t)$ at an elevation of $M_{\text{wave}}/F_{\text{wave}}$ above the MSL. F_{wave} is plotted against time in Fig. 15.

5.2 Analysis steps and initial conditions

The numerical simulation was performed through two analysis steps. In the first step, a geostatic equilibrium of the initial stresses was achieved assuming oedometric conditions. The vertical displacements were restricted on the bottom boundary as well as the horizontal displacements on the lateral boundaries. Thus, the initial stresses on the soil domain and pore pressure distribution are generated due to the self-weight of the model components and the hydrostatic pressure on the top surface. In the second step, the wind and wave time histories were applied on the structure under dynamic conditions. The total step time is 20 s with time increments of $\Delta t = 0.01$ s.

The initial conditions for the vertical stresses σ_{33} were computed using a saturated soil density of $\rho_{sat} = 1800$ kg/m^3 and considering an additional surcharge load equivalent to a 1 m column of soil to give numerical stability. The lateral earth pressure coefficient was set to $K_0 \approx 1 - \sin \varphi_c = 0.461$, and the horizontal initial stresses were obtained as $\sigma_{11} = \sigma_{22} = K_0\sigma_{33}$. Since the material is fully saturated, the initial pore pressure distribution corresponds to a hydrostatic state assuming a water intrinsic density of $\rho_w = 1000$ kg/m^3 and a 20 m water column above the mudline. Further on, the simulation is performed under undrained conditions, i.e., the pore water pressure p_w is obtained from Eq. 21, in which $K_w = 2.2 \times 10^5$ kPa is the water intrinsic bulk modulus, e the void ratio and $\underline{\varepsilon}$ the strain rate tensor.

$$\dot{p}_w = -K_w \frac{(1+e)}{e} tr\underline{\varepsilon} \tag{21}$$

Of course, one may improve simulations using coupled dynamic finite elements to consider consolidation effects, but this would increase the complexity of the model. The intergranular strain **h** and back-intergranular strain tensors **c** were initialized by setting them at their fully mobilized states pointing to the gravity direction, i.e., $h_{33} = -R$ and $c_{33} = -R/2$, where subindex 3 coincides with the vertical direction. The initial void ratio $e = e_0$ follows the Bauer's relation:

$$e_0 = r_0 e_{c0} \exp(-(3p/h_s)^{n_B}) \tag{22}$$

where r_0 is an additional constant to control the initial density and parameters e_{c0}, h_s, n_B are found in Table 1. An initial density with $r_0 = 0.85$ has been considered. This would simulate an initial relative density of $D_r = 0.731$ at the pile toe (30 m depth) and of $D_r = 0.649$ near the mudline.

5.3 FE model results

Contours showing only zones with very low mean (effective) stress $p < 3$ kPa, close to the liquefaction state $p \approx 0$, are plotted in Fig. 16. These contours correspond to the frame at the end of the simulations. For comparison purposes, two simulations have been analyzed: the first with $c_z = 0$ (no cyclic mobility extension) and the second with $c_z = 300$ (with cyclic mobility). The zone depicted in Fig. 16 corresponds to a section perpendicular to the wind and wave loads direction. The condition $p < 3$ kPa would, in principle, be met on the superficial soil. However, since the FE model considers surcharge load of 20 kPa at the ground surface to represent a small column of superficial soil, the condition $p < 3$kPa shows only the zones with reduced mean stress $p < 3$ kPa below the superficial soil. As expected, one may note that a larger zone with $p < 3$ kPa is exhibited by the model considering cyclic mobility ($c_z = 300$).

To gain insight about the results, plots of the development of the mean pressure p with time t, and shear stress σ_{23} versus mean pressure p are depicted in Fig. 17. They present the results of a point A, adjacent to the monopile at
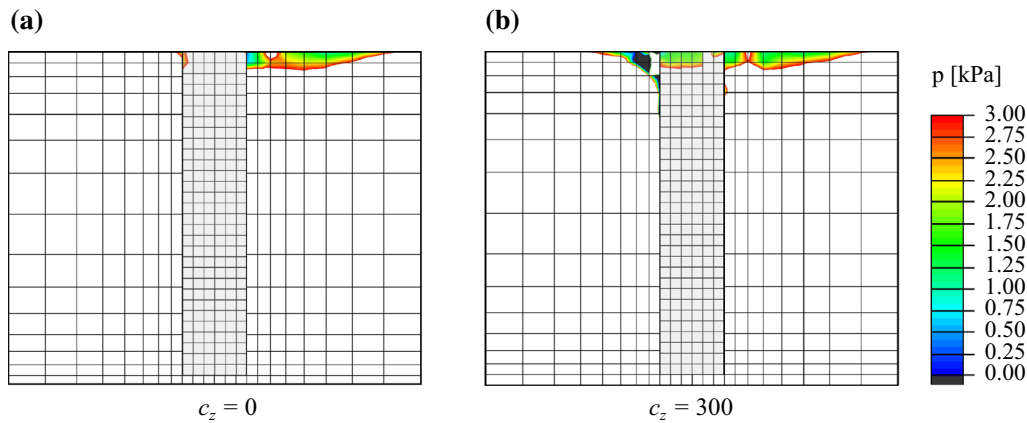
(a)   **(b)**

$c_z = 0$ $c_z = 300$

Fig. 16 FE simulation results. Liquefaction zones detected with $p < 3$ kPa. **a** $c_z = 0$, **b** $c_z = 300$

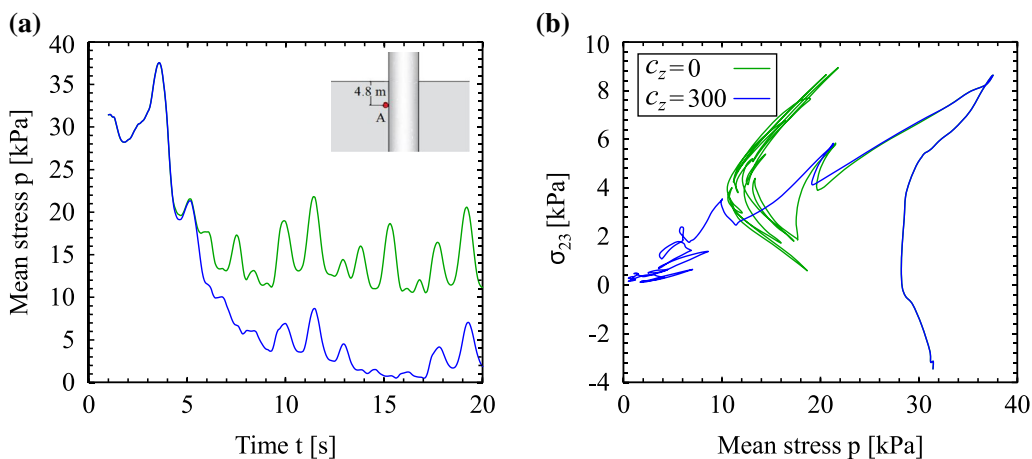**(a)**   **(b)**

Fig. 17 FE simulation results at point A ($z = 4.8$ m). **a** time history of the mean pressure p. **b** stress path: shear stress σ_{23} versus mean pressure p

4.8 m below the mudline, see sketch of the point position in Fig. 17. The results indicate that the reduction of the mean stress p is larger when considering cyclic mobility ($c_z = 300$). Notice that the effect of the cyclic mobility is evident after a time of 5 s.

6 Final remarks

An extension to an ISA-hypoplastic model for sands has been proposed to account for cyclic mobility effects. As by other models [1, 6, 21, 33, 39], the model is now able to reduce drastically the effective mean pressure by undrained cyclic loading. The mechanism to detect cyclic mobility paths was similar as in other works, but the way to account for this information on the constitutive model was different: contractant behavior on cyclic mobility paths was captured by modifying the pyknotropy and batotropy factors from the hypoplastic model denoted by f_e and f_b. In this way, the capabilities of the model related to the correct simulation of the stress–dilatancy ratio under drained tests

were maintained. The current modification requires the calibration of two additional parameters, which may be found by trial and error from a limited number of cyclic triaxial tests. Some simulation examples with cyclic undrained triaxial tests showed that the model captures well the cyclic mobility effect. In addition, a dynamic FE simulation of an offshore monopile subjected to environmental cyclic loading, showed that the new extension provides larger areas of reduced mean stress ($p < 3$ kPa) than the former model for same conditions.

Notation and conventions

The notation and convention of the present work is as follows: Italic fonts denote scalar magnitudes (e.g., a, b), bold lowercase letters denote vectors (e.g., $\mathbf{a}$, $\mathbf{b}$), bold capital letters denote second-rank tensors (e.g., $\mathbf{A}$, $\boldsymbol{\sigma}$), and special fonts are used for fourth-rank tensors (e.g., E, L). Indicial notation can be used to represent components of tensors (e.g., A_{ij}), and their operations follow the Einstein's summation convention. The Kronecker delta symbol is represented by δ_{ij}, i.e., $\delta_{ij} = 1$ when $i = j$ and $\delta_{ij} = 0$ otherwise. The symbol $\mathbf{1}$ denotes the Kronecker delta tensor ($1_{ij} = \delta_{ij}$). The unit fourth-rank tensor for symmetric tensors is denoted by I, where $\mathsf{I}_{ijkl} = \frac{1}{2}\left(\delta_{ik}\delta_{jl} + \delta_{il}\delta_{jk}\right)$. Multiplication with two dummy indices (double contraction) is denoted with a colon " : " (e.g., $\mathbf{A} : \mathbf{B} = A_{ij}B_{ij}$). The symbol "$\otimes$" represents the dyadic product (e.g., $\mathbf{A} \otimes \mathbf{B} = A_{ij}B_{kl}$). The brackets $\| \lfloor \rfloor \|$ extract the Euclidean norm (e.g., $\| \mathbf{A} \| = \sqrt{A_{ij}A_{ij}}$). Normalized tensors are denoted by $\overrightarrow{\lfloor \rfloor} = \frac{\lfloor \rfloor}{\|\lfloor \rfloor\|}$, or in general as $\lfloor \rfloor^{\rightarrow}$. The superscript $\lfloor \rfloor^{\mathrm{dev}}$ extracts the deviatoric part of a tensor (e.g., $\mathbf{A}^{\mathrm{dev}} = \mathbf{A} - \frac{1}{3}(\mathrm{tr}\mathbf{A})\mathbf{1}$). Components of the effective stress tensor $\boldsymbol{\sigma}$ or strain tensor $\boldsymbol{\varepsilon}$ in compression are negative. Roscoe variables are defined as $p = -\sigma_{ii}/3$, $q = \sqrt{\frac{3}{2}} \| \boldsymbol{\sigma}^{\mathrm{dev}} \|$, $\varepsilon_v = -\varepsilon_{ii}$ and $\varepsilon_s = \sqrt{\frac{2}{3}} \| \boldsymbol{\varepsilon}^{\mathrm{dev}} \|$. The stress ratio η is defined as $\eta = q/p$. The deviator stress tensor is defined as $\boldsymbol{\sigma}^{\mathrm{dev}} = \boldsymbol{\sigma} + p\,\mathbf{1}$ and the stress-ratio tensor with $\mathbf{r} = \boldsymbol{\sigma}^{\mathrm{dev}}/p = \sqrt{\frac{2}{3}}\eta\,\overrightarrow{\boldsymbol{\sigma}^{\mathrm{dev}}}$.

Empirical relation for shear degradation curve by Wichtmann and Triantafyllidis [47]

The empirical relation provided by Wichtmann and Triantafyllidis [47] is:

$$G_{\max} = 74000 \frac{1 + D_r}{(11.6 - D_r)^2}\left(\frac{p}{p_{\mathrm{atm}}}\right)^{0.48} p_{\mathrm{atm}} \tag{23}$$

with the relative density $D_r = (e_{\max} - e)/(e_{\max} - e_{\min})$ and the reference stress $p_{\mathrm{atm}} = 100$ kPa. For Karlsruhe fine sand $e_{\max} = 1.054$ and $e_{\min} = 0.677$. The secant shear modulus G_{sec} is computed with the empirical relation provided by Wichtmann and Triantafyllidis [47] :

$$\frac{G_{\mathrm{sec}}}{G_{\max}} = \frac{1}{1 + \Delta\gamma/\gamma_r(1 + a\exp(-\Delta\gamma/\gamma_r))} \tag{24}$$

where $\Delta\gamma$ is the shear strain amplitude, $a = 1.070\ln(c_u)$ is a constant, $\gamma_r = \tau_{\max}/G_{\max}$ is the reference strain, $\tau_{\max} = p\sin(\varphi_p)$ is the maximum shear stress and $\varphi_p = $

$34° \exp(0.27D_r^{1.8})$ is the peak friction angle. c_u is the uniformity coefficient ($c_u = D_{60}/D_{10}$). For Karlsruhe fine sand, $c_u = 1.5$ and therefore $a = 0.433$.

For drained triaxial conditions, the strain amplitude $\| \Delta\boldsymbol{\varepsilon} \|$ is computed with the following approximation $\| \Delta\boldsymbol{\varepsilon} \| = \sqrt{(\Delta\varepsilon_1)^2(1 + 2v^2)}$ where v is the Poisson ratio. For same conditions, it can be shown that the relation $\Delta\gamma = \Delta\varepsilon_1(1 + v)$ holds. For the computations with Karlsruhe fine sand, a value of $v = 0.3$ was used.

The resulting parameters for $e_0 = 0.85$ and $p = 200$ kPa are $\gamma_r = 9.29 \times 10^{-4}$, $G_{\max} = 130058$ kPa. For $e_0 = 0.85$ and $p = 300$ kPa are $\gamma_r = 1.14 \times 10^{-3}$ and $G_{\max} = 158002$ kPa.

ISA-hypoplastic model for sands

"Appendix C" presents a summary of the constitutive equations of the ISA-hypoplastic model. Details of the equations below are found in [11, 35, 49].

$$\dot{\boldsymbol{\sigma}} = \mathsf{M} : \dot{\boldsymbol{\varepsilon}} \tag{25}$$

$$\mathsf{M} = \begin{cases} m(\mathsf{L}^{\mathrm{hyp}} + \rho^{\chi}\mathbf{N}^{\mathrm{hyp}}\mathbf{N}) & \text{for } F_H = 0 \quad \text{(plastic)} \\ m_R\mathsf{L}^{\mathrm{hyp}} & \text{for } F_H < 0 \quad \text{(elastic)} \end{cases} \tag{26}$$

where $\mathsf{L}^{\mathrm{hyp}}$ and $\mathbf{N}^{\mathrm{hyp}}$ are the (fourth rank) linear and (second rank) nonlinear stiffness, respectively, $\mathbf{N} = (\mathbf{h} - \mathbf{c})^{\rightarrow}$ is the IS flow rule, m_R is a parameter, and ρ, m, χ and F_H are scalar functions defined in the sequel. The IS yield surface function F_H is defined as:

$$F_H = \| \mathbf{h} - \mathbf{c} \| - R/2 \tag{27}$$

where $\mathbf{h}$ is the IS tensor, $\mathbf{c}$ is the back-IS tensor, and R is a parameter. Factors m, y_h and ρ are defined as:

$$m = m_R + (1 - m_R)y_h \tag{28}$$

$$y_h = \rho^{\chi}\langle \mathbf{N} : \dot{\boldsymbol{\varepsilon}} \rangle \tag{29}$$

$$\rho = 1 - \frac{\|\mathbf{d}_b\|}{2R}, \quad \text{with} \quad \mathbf{d}_b = \mathbf{h}_b - \mathbf{h}, \quad \text{and} \quad \mathbf{h}_b = R\mathbf{N} \tag{30}$$

The evolution equation for the IS tensor $\mathbf{h}$ is:

$$\dot{\mathbf{h}} = \dot{\boldsymbol{\varepsilon}} - \dot{\lambda}_H\mathbf{N}, \quad \text{with} \quad \mathbf{N} = (\mathbf{h} - \mathbf{c})^{\rightarrow},$$
$$\text{and} \quad \dot{\lambda}_H = \frac{\langle \mathbf{N} : \dot{\boldsymbol{\varepsilon}} \rangle}{1 + \mathbf{N} : \bar{\mathbf{c}}} \tag{31}$$

where $\dot{\lambda}_H$ is the plastic multiplier of the IS model. The evolution equation for tensor $\mathbf{c}$ is:

$$\dot{\mathbf{c}} = \dot{\lambda}_H \bar{\mathbf{c}}, \quad \text{with} \quad \bar{\mathbf{c}} = \beta_h(\mathbf{c}_b - \mathbf{c})/R, \quad \text{and} \quad \mathbf{c}_b = (R/2)\overrightarrow{\dot{\boldsymbol{\varepsilon}}} \tag{32}$$

where β_h is a factor, which takes the value of $\beta_h = \beta_{hmax}$ for the condition $|\overrightarrow{\mathbf{h}_b} : \overrightarrow{\mathbf{d}_b}| = 0$, and $\beta_h = \beta_{h0}$ for $|\overrightarrow{\mathbf{h}_b} : \overrightarrow{\mathbf{d}_b}| = 1$.

$$\beta_h = \beta_{hmax} + (\beta_{h0} - \beta_{hmax})|\overrightarrow{\mathbf{h}_b} : \overrightarrow{\mathbf{d}_b}| \tag{33}$$

The internal variable $\dot{\varepsilon}_{acc}$ evolves according to:

$$\dot{\varepsilon}_{acc} = \frac{c_a}{R}(1 - y_h - \varepsilon_{acc}) \| \dot{\boldsymbol{\varepsilon}} \| \tag{34}$$

Function χ is defined as:

$$\chi = \chi_0 + \varepsilon_{acc}(\chi_{max} - \chi_0) \tag{35}$$

The equations of the reference hypoplastic model by Wolffersdorff [49] are given below:

$$\mathsf{L}^{hyp} = f_b f_e \frac{1}{\hat{\boldsymbol{\sigma}} : \hat{\boldsymbol{\sigma}}} (F^2 \mathsf{I} + a^2 \hat{\boldsymbol{\sigma}}\hat{\boldsymbol{\sigma}}) \tag{36}$$

$$\mathbf{N}^{hyp} = f_d f_b f_e \frac{Fa}{\hat{\boldsymbol{\sigma}} : \hat{\boldsymbol{\sigma}}} (\hat{\boldsymbol{\sigma}} + \hat{\boldsymbol{\sigma}}^{dev}) \tag{37}$$

$$
\begin{aligned}
f_e &= \left(\frac{e_c}{e}\right)^\beta \\
f_b &= \frac{h_s}{n_B}\left(\frac{1+e_i}{e_i}\right)\left(\frac{e_{i0}}{e_{c0}}\right)^\beta \left(-\frac{\mathrm{tr}\boldsymbol{\sigma}}{h_s}\right)^{1-n_B} \\
&\quad \left[3 + a^2 - \sqrt{3}a\left(\frac{e_{i0} - e_{d0}}{e_{c0} - e_{d0}}\right)^\beta\right]^{-1} \\
f_d &= \left(\frac{e - e_d}{e_c - e_d}\right)^\alpha
\end{aligned}
\tag{38}
$$

$$F = \sqrt{\frac{1}{8}\tan^2(\psi) + \frac{2 - \tan^2(\psi)}{2 + 2\sqrt{2}\tan(\psi)\cos(3\theta)}} - \frac{1}{2\sqrt{2}\tan(\psi)} \tag{39}$$

$$
\begin{aligned}
a &= \frac{\sqrt{3}(3 - \sin(\varphi_c))}{2\sqrt{2}\sin(\varphi_c)} \\
\tan\psi &= \sqrt{3}\|\hat{\boldsymbol{\sigma}}^{dev}\| \\
\cos(3\theta) &= \sqrt{6}\frac{\mathrm{tr}(\hat{\boldsymbol{\sigma}}^{dev}\hat{\boldsymbol{\sigma}}^{dev}\hat{\boldsymbol{\sigma}}^{dev})}{(\hat{\boldsymbol{\sigma}}^{dev} : \hat{\boldsymbol{\sigma}}^{dev})^{3/2}}
\end{aligned}
\tag{40}
$$

$$
\begin{aligned}
e_i &= e_{i0}\exp(-(3p/h_s)^{n_B}) \\
e_d &= e_{d0}\exp(-(3p/h_s)^{n_B}) \\
e_c &= e_{c0}\exp(-(3p/h_s)^{n_B})
\end{aligned}
\tag{41}
$$

The set of parameters are φ_c, h_s, n_B, e_{i0}, e_{c0}, e_{d0}, α, β, R, χ_0, χ_{max}, β_{h0}, β_{hmax}, c_a. The state variables are e, $\mathbf{c}$, $\mathbf{h}$ and ε_{acc}.
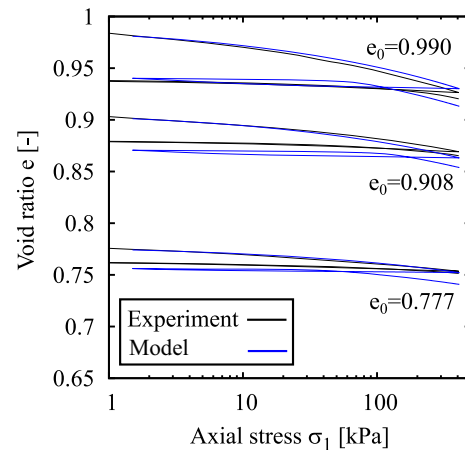

Fig. 18 Simulation of oedometer compression with one cycle unloading–reloading with different initial void ratios

Inspection of hypoplastic flow rule tensor m

Substitution of Eqs. 36 and 37 in tensor $\mathbf{m} = -(\mathsf{L}^{hyp})^{-1} : \mathbf{N}^{hyp}$ gives (see procedure in [29]):

$$
\begin{aligned}
\mathbf{m} &= -(\mathsf{L}^{hyp})^{-1} : \mathbf{N}^{hyp} \\
&= -\frac{1}{F^2}\left[\mathsf{I} - \frac{\hat{\boldsymbol{\sigma}}\hat{\boldsymbol{\sigma}}}{(F/a)^2 + \hat{\boldsymbol{\sigma}} : \hat{\boldsymbol{\sigma}}}\right] : f_d a^2 \left(\frac{F}{a}\right)(\hat{\boldsymbol{\sigma}} + \hat{\boldsymbol{\sigma}}^{dev})
\end{aligned}
\tag{42}
$$

Splitting tensor $\mathbf{m}$ into volumetric and deviatoric components $\mathbf{m}^{vol} = \mathsf{I}^{vol} : \mathbf{m}$ and $\mathbf{m}^{dev} = \mathsf{I}^{dev} : \mathbf{m}$, where $I^{vol}_{ijkl} = 1/3\delta_{ij}\delta_{kl}$ and $I^{dev}_{ijkl} = I_{ijkl} - I^{vol}_{ijkl}$ gives:

$$\mathbf{m}^{vol} = \mathsf{I}^{vol} : \mathbf{m} = \frac{1}{3\sqrt{3}}\frac{a}{F}f_\sigma\mathbf{1} \tag{43}$$

$$\mathbf{m}^{dev} = \mathsf{I}^{dev} : \mathbf{m} = \frac{a}{F}(f_\sigma + 1)\hat{\boldsymbol{\sigma}}^{dev} \tag{44}$$

Where fuction f_σ is defined as:

$$f_\sigma = \frac{(F/a)^2 - \|\hat{\boldsymbol{\sigma}}^{dev}\|}{(F/a)^2 + \|\hat{\boldsymbol{\sigma}}\|} \tag{45}$$

Simulations of monotonic loading

In this "Appendix", some simulations of the Karlsruhe fine sand under monotonic loading are presented. Simulations versus experiments are shown in Figs. 18 and 19. Parameters of Table 1 were used for the simulations.
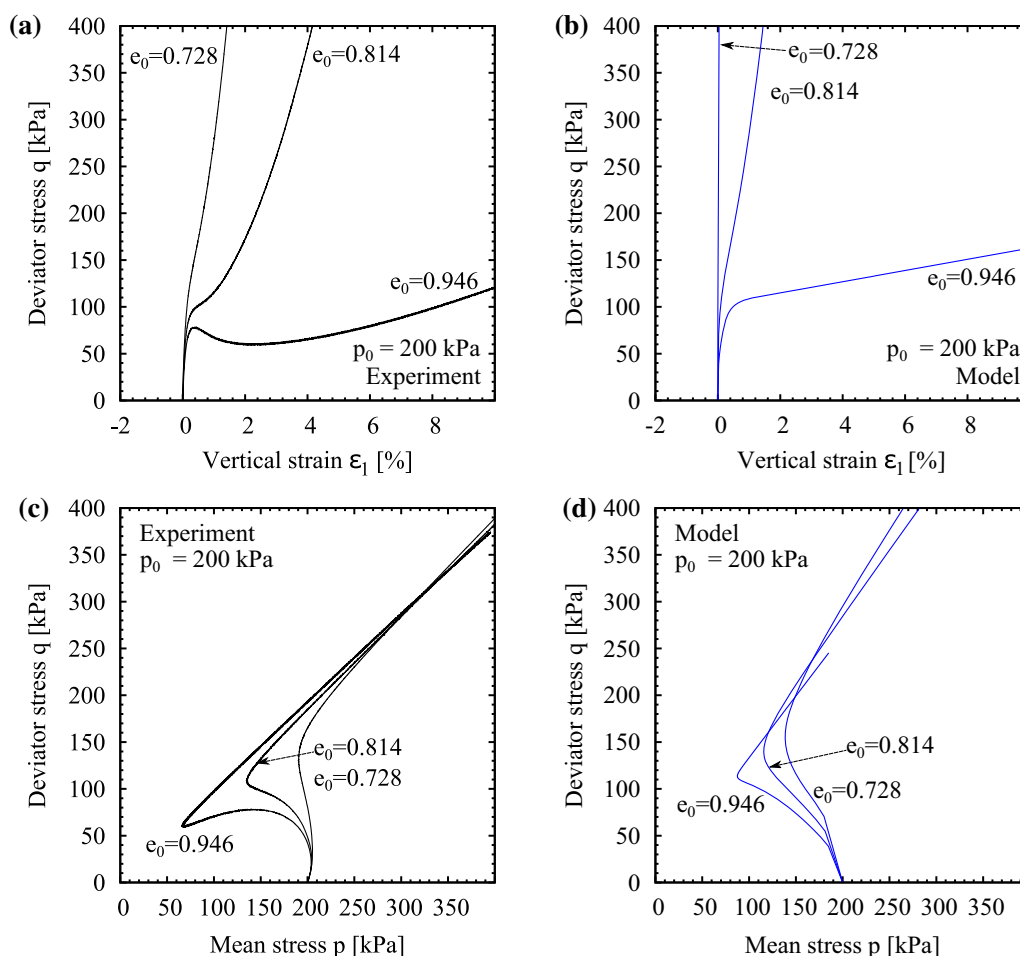
Fig. 19 Simulation of undrained triaxial tests with different initial void ratios

References

1. Andrianopoulos K, Papadimitriou A, Bouckovalas G (2010) Bounding surface plasticity model for the seismic liquefaction analysis of geostructures. Soil Dyn Earthq Eng 30(10):895–911

2. API (American Petroleum Institute) (2014) Recommended practice for planning, designing and constructing fixed offshore platforms: working stress design. American Petroleum Institute, Washington

3. Arany L, Bhattacharya S, Macdonald J, Hogan SJ (2017) Design of monopiles for offshore wind turbines in 10 steps. Soil Dyn Earthq Eng 92:126–152

4. Boulanger R, Ziotopoulou K (2012) Pm4sand (version 2): a sand plasticity model for earthquake engineering applications. Technical report, University of California, Center for geotechnical modeling department of civil and environmental engineering, Davis, California, USA

5. Chang CS, Yin Z-Y (2010) Modeling stress-dilatancy for sand under compression and extension loading conditions. J Eng Mech 136(6):777–786

6. Dafalias Y, Manzari M (2004) Simple plasticity sand model accounting for fabric change effects. J Eng Mech ASCE 130(6):634–662

7. Das A, Bajpai P (2018) A hypo-plastic approach for evaluating railway ballast degradation. Acta Geotechnica 13(5):1085–1102

8. Devis-Morales A, Montoya-Sánchez RA, Bernal G, Osorio AF (2017) Assessment of extreme wind and waves in the Colombian Caribbean Sea for offshore applications. Appl Ocean Res 69:10–26

9. Fuentes W (2014) Contributions in mechanical modelling of fill materials. Schriftenreihe des Institutes für Bodenmechanik und Felsmechanik des Karlsruher Institut für Technologie, Heft 179

10. Fuentes W, Tafili M, Triantafyllidis T (2018) An isa-plasticity-based model for viscous and non-viscous clays. Acta Geotechnica 13(2):367–386

11. Fuentes W, Triantafyllidis T (2015) ISA model: A constitutive model for soils with yield surface in the intergranular strain space. Int J Numer Anal Meth Geomech 39(11):1235–1254

12. Fuentes W, Triantafyllidis T, Lascarro C (2017) Evaluating the performance of an isa-hypoplasticity constitutive model on problems with repetitive loading. In: Triantafyllidis T (ed) Holistic simulation of geotechnical installation processes, volume 82 lecture notes in applied and computational mechanics. Springer, Berlin, pp 341–362

13. Gasch R, Twele J (eds) (2012) Calculation of performance characteristics and partial load behaviour, chapter 6. Springer, Berlin, pp 208–256

14. Hansen MOL (2008) 1D momentum theory for an ideal wind turbine, chapter 4. Earthscan Publications Ltd, London, pp 27–40

15. Herle I, Kolymbas D (2004) Hypoplasticity for soils with low friction angles. Comput Geotech 31(5):365–373

16. Jonkman J, Butterfield S, Musial W, Scott G (February 2009) Definition of a 5-mw reference wind turbine for offshore system development. Technical report, National Renewable Energy Laboratory (NREL)

17. Kolymbas D (1991) Computer-aided design of constitutive laws. Int J Numer Anal Methods Geomech 8(15):593–604

18. Kolymbas D, Herle I (2005) Hypoplasticity as a constitutive framework for granular soils. In: ASCE, pp 257–289

19. Kuhn MR, Renken HE, Mixsell AD, Kramer SL (2014) Investigation of cyclic liquefaction with discrete element simulations. J Geotech Geoenviron Eng 140(12):04014075

20. Lade P, Ibsen L (1997) A study of the phase transformation and the characteristic lines of sand behaviour. geotechnical engineering group. Published In: Proceedings of international symposium on deformation and progressive failure in geomechanics, Nagoya, Japan, pp 353–359

21. LeBlanc C, Hededal O, Ibsen LB (2008) A modified critical state two-surface plasticity model for sand—theory and implementation. Technical report, Aalborg University, Department of Civil Engineering Water and Soil, Denmark

22. Li X, Dafalias Y (2000) Dilatancy for cohesionless soils. Géotechnique 50(4):449–460

23. Manwell JF, McGowan JG, Rogers AL (2009) Wind characteristics and resources, chapter 2. Wiley, Hoboken, pp 23–90

24. Masin D (2005) A hypoplastic constitutive model for clays. Int J Numer Anal Methods Geomech 29(4):311–336

25. Masin D, Herle I (2005) State boundary surface of a hypoplastic model for clays. Comput Geotech 32(6):400–410

26. Matsuoka H, Nakai T (1977) Stress-strain relationship of soil based on the SMP. In: Proceedings of speciality session 9, IX international conference on soil mechanics found Engineering, Tokyo, pp 153–162

27. Morison JR, Johnson JW, Schaaf SA (1950) The force exerted by surface waves on piles. J Pet Technol 2:149–154

28. Ng T, Dobry R (1994) Numerical simulations of monotonic and cyclic loading of granular soil. J Geotech Eng 120(2):388–403

29. Niemunis A (2003) Extended hypoplastic models for soils. Habilitation, Schriftenreihe des Institutes für Grundbau und Bodenmechanil der Ruhr-Universit"at Bochum, Germany, Heft 34

30. Niemunis A, Grandas C, Wichtmann T (2016) Peak stress obliquity in drained and undrained sands. Simulations with neo-hypoplasticity. Springer International Publishing, Cham, pp 85–114

31. Niemunis A, Herle I (1997) Hypoplastic model for cohesionless soils with elastic strain range. Mech Cohes Frict Mater 2(4):279–299

32. NRELs National Wind Technology Center (2018) Nrel 5-mw reference turbine - cp, cq, ct coefficients. https://wind.nrel.gov/forum/wind/viewtopic.php?f=2&t=582

33. Oka F, Kimoto S (2018) A cyclic elastoplastic constitutive model and effect of non-associativity on the response of liquefiable sandy soils. Acta Geotechnica 13(6):1283–1297

34. Osorio AF, Montoya RD, Ortiz JC, Peláez D (2016) Construction of synthetic ocean wave series along the colombian caribbean coast: a wave climate analysis. Appl Ocean Res 56:119–131

35. Poblete M, Fuentes W, Triantafyllidis T (2016) On the simulation of multidimensional cyclic loading with intergranular strain. Acta Geotechnica 11(6):1263–1285

36. Pradhan T, Tatsuoka F, Sato Y (1989) Experimental stress-dilatancy relations of sand subjected to cyclic loading. Soils Found 29(1):45–64

37. Sitharam TG, Dinesh SV (2003) Numerical simulation of liquefaction behaviour of granular materials using discrete element method. J Earth Syst Sci 112(3):479

38. Sitharam TG (2003) Discrete element modelling of cyclic behaviour of granular materials. Geotech Geol Eng 21(4):297–329

39. Taiebat M, Jeremic B, Dafalias Y, Kaynia A, Cheng Z (2010) Propagation of seismic waves through liquefied soils. Soil Dyn Earthq Eng 30:236–257

40. van der Tempel J (2006) Design of support structures for offshore wind turbines. PhD thesis, Delft University of Technology, Delft, Netherlands

41. Villalobos Jara FA (2006) Model testing of foundations for offshore wind turbines. PhD thesis, Oxford University, UK, United Kingdom

42. Vugts JH, van der Tempel J, Schrama EA (2001) Hydrodynamic loading on monotower support structures for preliminary design. In: Proceedings of special topic conference on offshore wind energy, Brussels, Belgium

43. Wang R, Fu P, Zhang J, Dafalias Y (2016) Dem study of fabric features governing undrained post-liquefaction shear deformation of sand. Acta Geotechnica 11(6):1321–1337

44. Wang S, Wei W, Peng C, He X, Cui D (2018) Numerical integration and FE implementation of a hypoplastic constitutive model. Acta Geotechnica 13(6):1265–1281

45. Wegener D, Herle I (2014) Prediction of permanent soil deformations due to cyclic shearing with a hypoplastic constitutive model. Geotechnik 37(2):113–122

46. Weifner T, Kolymbas D (2007) A hypoplastic model for clay and sand. Acta Geotechnica 2(2):103–112

47. Wichtmann T, Triantafyllidis T (2014) Stiffness and damping of clean quartz sand with various grain-size distribution curves. J Geotech Geoenviron Eng 140(3):1–4

48. Wichtmann T, Triantafyllidis T (2016) An experimental database for the development, calibration and verification of constitutive models for sand with focus to cyclic loading: part i–tests with monotonic loading and stress cycles. Acta Geotechnica 11(4):739–761

49. Wolffersdorff A (1996) A hypoplastic relation for granular materials with a predefined limit state surface. Mech Cohes Frict Mater 1(3):251–271

50. Wu W (1992) Hypoplastizität als mathematisches modell zum mechanischen Verhalten von Böden und Schöttstoffen. Phd thesis, Universität Karlsruhe, Germany. Institut für Boden- und Felsmechanik, Habilitation, Heft 129

51. Wu W, Bauer E (1994) A simple hypoplastic constitutive model for sand. International Journal for Numerical and Analytical Methods in Geomechanics 18(12):833–862

52. Wu W, Niemunis A (1996) Failure criterion, flow rule and dissipation function derived from hypoplasticity. Mechanics of Cohesive-Frictional Materials 1(2):145–163

53. Yin Z-Y, Chang CS (2011) Stress-dilatancy behavior for sand under loading and unloading conditions. International Journal for Numerical and Analytical Methods in Geomechanics 37(8):855–870